Remote Sensing of Environment 284 (2023) 113341

Contents lists available at ScienceDirect

Remote Sensing of Environment

journal homepage: www.elsevier.com/locate/rse

# A simple approach to enhance the TROPOMI solar-induced chlorophyll fluorescence product by combining with canopy reflected radiation at near-infrared band

Xinjie Liu[a,b], Liangyun Liu[a,b,*], Cédric Bacour[c], Luis Guanter[d], Jidai Chen[a,b], Yan Ma[a,b], Ruonan Chen[a,b], Shanshan Du[a,b]

[a] International Research Center of Big Data for Sustainable Development Goals, Beijing 100094, China
[b] Key Laboratory of Digital Earth Science, Aerospace Information Research Institute, Chinese Academy of Sciences, Beijing 100094, China
[c] Laboratoire des Sciences du Climat et de l'Environnement, LSCE/IPSL, CEA-CNRS-UVSQ, Université Paris-Saclay, Gif-sur-Yvette F-91191, France.
[d] Research Institute of Water and Environmental Engineering (IIAMA), Universitat Politècnica de València, Valencia, Spain

ARTICLE INFO

Edited by Jing M. Chen

*Keywords:*
Solar-induced chlorophyll fluorescence (SIF)
Near-infrared radiation reflected by vegetation (NIRvP)
Gross primary productivity (GPP)
Multi-source data combination

ABSTRACT

Satellite-based data of solar-induced chlorophyll fluorescence (SIF) and the near-infrared radiation reflected by vegetation (NIRvP) are being increasingly used for the estimation of vegetation gross primary product (GPP) at the global scale. Although SIF contains more physiological information than NIRvP, NIRvP can have higher data quality and spatio-temporal resolution. Therefore, the two variables can be considered complementary for GPP monitoring. Here, we propose a simple framework to combine SIF and NIRvP data from different data sources to generate an enhanced SIF product (eSIF). The original SIF data comes from the TROPOMI instrument onboard the Sentinel-5P mission, whereas NIRvP data are derived from MODIS spectral reflectance and ERA5 reanalysis data. The resulting eSIF product has a spatial resolution of 0.05° and a temporal resolution of 8 days, as well as a higher signal-to-noise ratio and a lower angular dependency than the original TROPOMI SIF data. Our results demonstrate that eSIF has similar spatial patterns to the original SIF but is more spatially continuous and less noisy. Comparisons with the FLUXCOM global GPP product show that eSIF has a more universal relationship with GPP than NIRvP for different grass/crop plant functional types (the coefficients of variation are 18.9% for slopes of GPP to eSIF and 27.3% for slopes of GPP to NIRvP), but NIRvP outperforms eSIF for tracking GPP for forest PFTs exclude BoENF. Moreover, eSIF is able to better track the seasonal variations in GPP related to environmental stresses. This study highlights that our methodology based on the combination of SIF and NIRvP is a promising approach for better monitoring of GPP.

## 1. Introduction

Solar-induced chlorophyll fluorescence (SIF) is emitted by chlorophyll-*a* molecules in the light reaction of photosynthesis, andit has been widely used as a good proxy of vegetation gross primary productivity (GPP). With the fast development of advanced satellite-based sensors and SIF retrieval algorithms in recent years, SIF has shown great potential for GPP monitoring at the global scale (e.g., Frankenberg et al., 2011; Guanter et al., 2014; Porcar-Castell et al., 2014; Joiner et al., 2014; Walther et al., 2016; Sun et al., 2017; Porcar-Castell et al., 2021; Li and Xiao, 2022; Pickering et al., 2022; Cui et al., 2022).

The SIF observed at canopy level can be expressed as follows (Guanter et al., 2014):

$$\mathrm{SIF} = \mathrm{PAR} \times f\mathrm{APAR} \times \Phi_F \times f_{esc} \tag{1}$$

where PAR is the photosynthetically active radiation, *f*APAR is the fraction of absorbed PAR (APAR), $\Phi_F$ is the SIF yield inside leaves, and $f_{esc}$ is the canopy SIF escape probability, which represents the fraction of total emitted SIF photons that can be observed at the top of canopy. PAR, *f*APAR, and $f_{esc}$ are related to incident radiation, canopy structure, and leaf pigments, while $\Phi_F$ is related to the physiological status of vegetation.

According to Zeng et al. (2019), $f_{esc}$ in the near-infrared band can be estimated as follows:

---

[*] Corresponding author at: International Research Center of Big Data for Sustainable Development Goals, Beijing 100094, China.
*E-mail address:* liuly@radi.ac.cn (L. Liu).

https://doi.org/10.1016/j.rse.2022.113341
Received 27 February 2022; Received in revised form 12 October 2022; Accepted 29 October 2022

$$f_{esc} \approx \frac{\text{NIRv}}{f\text{APAR}} \tag{2}$$

where NIRv is the near-infrared reflectance of vegetation and is calculated as the product of the normalized difference vegetation index (NDVI) and the near-infrared reflectance ($R_{NIR}$) (Badgley et al., 2017). Consequently, SIF at near-infrared band can be expressed as:

$$\text{SIF} \approx \text{PAR} \times \text{NIRv} \times \Phi_F = \text{NIRvP} \times \Phi_F \tag{3}$$

where NIRvP is the product of PAR and NIRv, and represents the vegetation reflected radiation at the near-infrared band (Dechant et al., 2022).

The uncertainties in the SIF–GPP relationship are mainly controlled by variation in $\Phi_F$, $f_{esc}$, and the light use efficiency for photosynthesis (LUE) (Wieneke et al., 2018; Wohlfahrt et al., 2018; Porcar-Castell et al., 2021; Liu et al., 2021). The different contributions of $\Phi_F$ and $f_{esc}$ to the SIF–GPP relationship have been discussed in several recent studies (Dechant et al., 2020; Liu et al., 2020; Wu et al., 2020; Kim et al., 2021; Kimm et al., 2021; Xu et al., 2021; Yang et al., 2021; Zhang et al., 2021b; Dechant et al., 2022).

As both chlorophyll fluorescence and photosynthesis occur at the photosystem level inside leaves, one could argue that the influence of $f_{esc}$ should be removed before linking SIF to GPP (Porcar-Castell et al., 2014; Yang et al., 2019; Zeng et al., 2019; Gu et al., 2019; Liu et al., 2019; Zhang et al., 2020; Porcar-Castell et al., 2021). However, as reported by Dechant et al. (2020), for crops, whereas the relationship between SIF and APAR is indeed improved after the removal of the influence of $f_{esc}$ on SIF, the correlation between SIF and GPP decreases, which indicates that $f_{esc}$ positively contributes to the SIF–GPP relationship. The reason is related to the covariation in $f_{esc}$ and LUE but little variation in $\Phi_F$ at both seasonal and diurnal scales for crops (Liu et al., 2020; Yang et al., 2021). Consequently, NIRvP is found satisfactory for GPP estimation for specific crops. Similar results have also been reported by other studies on various ecosystems including crops, grassland, wetland, and savanna, etc. (e.g., Baldocchi et al., 2020; Liu et al., 2020; Wu et al., 2020). The good relationship between satellite-based NIRvP and GPP has also been reported (e.g. Jiang et al., 2021; Kong et al., 2022). Dechant et al. (2022) comprehensively investigated the relationship between SIF and NIRvP using ground-based, airborne, and satellite-based, observations and confirmed that NIRvP is a robust structural proxy of SIF. The authors also reported the potential of NIRvP for better monitoring of GPP than SIF due to its higher data quality (including data availability, spatio-temporal resolution, and signal quality). It needs to be noted that both NIRvP and $f_{esc}$ are influenced by the bi-directional effect of canopy reflectance, whose impact is likely more important for wide-swath instruments like TROPOMI which may have large variation in view zenith angles, and therefore require to be corrected (Liu et al., 2019; Zeng et al., 2022a).

On the contrary, the importance of $\Phi_F$ to the SIF–GPP relationship is prominent when the photosynthesis physiological status is affected by abiotic changes and stresses. For evergreen needleleaf forest (ENF), the seasonal variation in the canopy structure and leaf pigments is relatively small, which results in small seasonal variation of NDVI and APAR. However, the results in Magney et al. (2019) showed that $\Phi_F$ might be able to capture the seasonal variation in LUE for ENF, and Kim et al. (2021) showed that the relationship between $\Phi_F$ and LUE for ENF was non-linear. Using airborne HyPlant images, Zeng et al. (2022a) reported that $\Phi_F$ is able to respond to the variation in photosynthesis status caused by light, temperature, and water. Turner et al. (2021) reported that SIF from TROPOMI observations better tracks decreasing GPP due to the extreme drought in California in 2018 than NIRv, and confirmed that SIF is a measure of photosynthetic activity as opposed to photosynthetic capacity (Walther et al., 2016). These studies highlight the unique advantages of SIF (specifically, the physiological information contained in $\Phi_F$) for photosynthesis monitoring.

Unfortunately, the unique physiological information contained in SIF is concealed by the high retrieval error in practice, especially for space-borne SIF data, which is a major drawback for SIF as a proxy of GPP (Ryu et al., 2019; Peng et al., 2020; Dechant et al., 2022). The intensity of the SIF signal is weak compared to the reflected radiation (Meroni et al., 2009). SIF can only be retrieved from spectral measurements with very high spectral resolution (sub-nanometer level) to capture the solar or telluric atmospheric absorption lines in the red and far-red bands (Meroni et al., 2009). In practice, high spectral resolution monitoring usually goes together with low spatial/temporal resolution sampling and a low signal-to-noise ratio (SNR) (Liu et al., 2015). And for now, space-borne sensors which have potential for SIF retrieval are mostly initially dedicated to the observation of atmospheric parameters, and hence usually have coarse spatial resolution. Moreover, there are usually relatively large uncertainties in SIF retrieval, caused by a lack of robustness in algorithms, atmospheric radiation transfer effects, etc. (Damm et al., 2011; Liu and Liu, 2014; Damm et al., 2015; Mohammed et al., 2019). Although several SIF datasets based on different sensors/ retrieval algorithms have emerged over the past decade (e.g. Joiner et al., 2011; Frankenberg et al., 2011; Joiner et al., 2016; Köhler et al., 2018; Du et al., 2018; Guanter et al., 2021), the potential of global SIF datasets remains largely limited by their spatio-temporal resolution and noise (random errors). For example, OCO-2 provides SIF estimates with a footprint size of ~2 km, but its narrow swath prevents any global coverage (Köhler et al., 2018; Sun et al., 2018); the GOME-2 SIF product has the longest time series (since 2007) with an almost daily coverage, but at a coarse spatial resolution of approximately 0.5° (Joiner et al., 2016; Köhler et al., 2015; Parazoo et al., 2019). The TROPOMI SIF product outperforms previous satellite-based SIF products by combining a relatively high spatial resolution (up to ~$3.5 \times 5.5$ km$^2$ at nadir) and a wide swath, resulting in an almost daily global coverage of observations (Guanter et al., 2015; Köhler et al., 2018; Guanter et al., 2021). However, multi-day aggregations are still necessary for a satisfying global coverage with a spatial resolution of approximately 5 km to deal with the influence of cloud cover, an enlarged footprint size with an increased view zenith angle, and failures in SIF retrievals.

To overcome the limitations caused by the low spatial resolution and large noise in current satellite-based SIF products, several reconstructed SIF products have been proposed in recent years, such as CSIF (Zhang et al., 2018a), RSIF (Gentine and Alemohammad, 2018), GOSIF (Li and Xiao, 2019), downscaled SIF (Duveiller and Cescatti, 2016; Duveiller et al., 2020; Ma et al., 2022), SIFnet (Gensheimer et al., 2022), etc. These works use machine learning methods to model the relationship between satellite observed SIF and multi-source predictor variables including reflectance, meteorological parameters, and vegetation types, and consequently, use these predictor variables to reconstruct “SIF” product with high spatial resolution, long time series and high data quality. However, although these products have shown strong correlation with both original SIF and GPP at global scale, in strict sense, they are not real SIF, because it is still not clear whether the unique information contained in SIF (especially in $\Phi_F$) could be well predicted using other variables. Moreover, these machine learning methods for SIF reconstruction is relatively complex and intransparent in mechanism. Therefore, the reconstructed or simulated SIF products could not provide convincing information on the quantitative relationship between SIF and GPP and the mechanism behind it.

Another limitation of SIF-based GPP estimation is related to the mismatch between the temporal scale of SIF and GPP observations (Zhang et al., 2018b). SIF is an instantaneous parameter that varies with the incoming radiation, whereas GPP is usually used as an accumulated parameter during a certain period. Therefore, temporal upscaling (e.g., from instantaneous to daily average) of SIF is needed for better GPP monitoring (Zhang et al., 2018b; Hu et al., 2021). Several studies have performed temporal upscaling of instantaneous SIF data to daily averaged values based on the variation of the solar zenith angle (Frankenberg et al., 2011; Joiner et al., 2016; Köhler et al., 2018; Zhang et al., 2018b), which is used as a proxy of incident radiation under clear sky conditions. The popularly used OCO-2 (Frankenberg et al., 2014; Sun et al., 2018), GOME-2 (Köhler et al., 2015; Joiner et al., 2016), and TROPOMI (Köhler et al., 2018; Guanter et al., 2021) SIF products also provide daylength-corrected SIF values or daily correction factors. However, the solar zenith angle is not able to represent the weather-caused variations in incoming radiation. Hence, Hu et al. (2021) proposed an improved temporal upscaling method for GOME-2 SIF based on PAR from the MERRA-2 (Modern-Era Retrospective analysis for Research and Applications, Version 2) reanalysis dataset.

To sum up, SIF and NIRvP have complementary advantages for monitoring photosynthesis of terrestrial ecosystems. Although SIF contains more physiological information than NIRvP, NIRvP can have higher data quality and spatio-temporal resolution. And the existing reconstructed SIF products still suffer from the complexity and intransparent mechanism of the methods they based. Therefore, it is necessary to investigate the possibility to make comprehensive use of SIF and NIRvP to generate a new enhanced SIF product, which can keep the key information of original SIF and has improved data quality. The aims of this study are: (1) to introduce a simple framework with clear mechanism to combine SIF and NIRvP, and generate an enhanced SIF product (eSIF) with a spatial resolution of 0.05° and a temporal resolution of 8 days; (2) to compared the performance of the enhanced SIF (eSIF), the original SIF, and NIRvP for monitoring GPP across different plant functional types (PFTs); (3) to investigate the complementarity of NIRvP and SIF for monitoring GPP.

## 2. Materials and methods

### 2.1. Theoretical framework

According to the different characteristics of SIF and NIRvP as introduced above, we suggest below a framework to enhance the potential of SIF data for GPP monitoring based on Eqs. (1)–(3).

First, several recent studies have shown that NIRvP is closely related to SIF across wide spatial and temporal scales and could represent most of the information of SIF (Dechant et al., 2020; Dechant et al., 2022; Gensheimer et al., 2022), suggesting that $\Phi_F$ is relatively stable, especially for the same PFT. Hence, because the errors associated with NIRvP are much smaller than in SIF estimates, it would be an efficient way to improve the quality of SIF signals by smoothing $\Phi_F$ in the spatial or temporal dimensions. Moreover, it would be possible to determine daily averaged SIF values from instantaneous SIF estimates using actual daily averaged PAR (instead of daily averaging based on solar zenith angle). Finally, as PAR and $\Phi_F$ have no directional effect, the directional effect for the observed SIF could be normalized by the bi-directional normalization of NIRv or $R_{NIR}$(e.g., by kernel-driven method) (Zeng et al., 2022a). A potential-enhanced SIF product (named eSIF hereafter) maximizing the information of SIF, NIRv, and PAR could then be generated, relying on multi-source datasets to guarantee the most satisfying quality for each parameter. Fig. 1 shows a simple scheme for the generation of eSIF.

### 2.2. Datasets

#### 2.2.1. TROPOSIF product

The satellite-based SIF product retrieved from TROPOspheric Monitoring Instrument (TROPOMI) onboard Sentinel-5 Precursor, named TROPOSIF (v2.1 L2B) (Guanter et al., 2021), in 2019 was used. The L2B product consists of valid SIF estimates (ungridded, instantaneous values) within each day (Guanter et al., 2021). SIF retrieval was conducted using a principal component analysis-based data-driven method and was applied to two fitting windows (743–758 and 735–758 nm). In this study, only the "baseline" SIF product (743–758 nm, similar to the product of Köhler et al. (2018)) was used, as recommended by Guanter et al. (2021), and those observations with a cloud fraction higher than 0.2, view zenith angle larger than 60° and solar zenith angle larger than 70° were excluded.

Moreover, the TROPOSIF product also provides top-of-atmosphere (TOA) radiance (averaged within 743–758 nm), which is fully concomittant with SIF estimates, and is used for the estimation of $\Phi_F$ (see Section 2.3.1).

#### 2.2.2. MODIS surface reflectance

Although TROPOSIF products also contain surface reflectance (centered at 665, 680, 712, 741, 755, 773, and 781 nm with spectral windows of 3 nm), it is neither atmospherically nor directionally corrected. As the influence of atmosphere in the red band is not neglectable and the wide swath of TROPOMI can lead to large view zenith angles, which in turns may impact the surface reflectance estimates in TROPOSIF, we used the MODIS Nadir Bidirectional Reflectance Distribution Function (BRDF)-Adjusted Reflectance (NBAR) dataset (MCD43C4 v6.1) product (Schaaf, 2015) (https://lpdaac.usgs.gov/products/mcd43c4v006/) for the calculation of NDVI and NIRv. The MCD43C4 dataset is produced daily using a combination of Terra and Aqua MODIS data in a 16-day moving window, and the spatial resolution is 0.05°.

#### 2.2.3. ERA5-land reanalysis dataset

The land component of the fifth generation of the European ReAnalysis (ERA5-Land) dataset produced by the European Centre for Medium-Range Weather Forecasts (ECMWF) (Muñoz-Sabater et al., 2021), which is regarded as a state-of-the-art global reanalysis dataset for land applications, was used for the collection of the radiation and meteorological parameters needed in this study. The ERA5-Land dataset has a temporal resolution of one hour and a horizontal spatial resolution of 0.1°; it was linearly interpolated to 0.05° resolution to match the TROPOSIF and MCD43C4 datasets.

In this study, the daily averaged PAR was estimated using the all-sky surface shortwave radiation ($R_s$). The hourly $R_s$ of 24 h in one day was averaged and converted into PAR using a factor of 0.46 (Jacovides et al.,

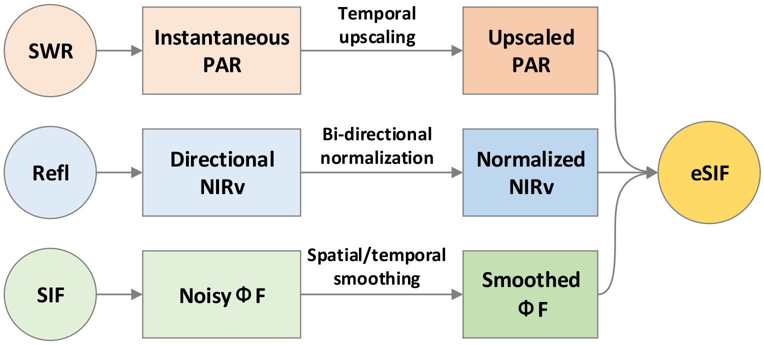

**Fig. 1.** Scheme for the generation of eSIF, combining information of SIF and NIRvP. SWR stands for shortwave radiation, and Refl stands for reflectance.

2003; Ryu et al., 2018). The factor would increase slightly for overcast sky condition (less than ~10%), and the influence was neglected in this study.

The surface pressure ($P$; in the unit of hPa), 2 m temperature ($T_a$; in the unit of degrees Celsius), and 2 m dewpoint temperature (in the unit of degrees Celsius) were used for calculation of the atmospheric vapor pressure deficit (VPD; in the unit of hPa) using the following equations (Buck, 1981; Yuan et al., 2019):

$$\mathrm{VPD} = \mathrm{SVP} - \mathrm{AVP} \tag{4}$$

$$\mathrm{AVP} = 6.112 \times f_w \times exp\left(\frac{17.67T_d}{T_d + 243.5}\right) \tag{5}$$

$$\mathrm{SVP} = 6.112 \times f_w \times exp\left(\frac{17.67T_a}{T_a + 243.5}\right) \tag{6}$$

$$f_w = 1 + 7 \times 10^{-4} + 3.46 \times 10^{-6}P \tag{7}$$

where SVP and AVP are the saturated and actual vapor pressure, respectively, in the unit of hPa; $f_w$ is a fitted enhancement factor defined as the ratio of the saturation vapor pressure of moist air to that of pure water vapor.

### 2.2.4. FLUXCOM global GPP product

We used the FLUXCOM global GPP product (RS_V006), which relies on machine learning methods to upscale tower-based eddy covariance measurements using MODIS remote sensing data (Jung et al., 2019; Jung et al., 2020). The FLUXCOM (RS_V006) GPP product has a temporal resolution of 8 days and a spatial resolution of 0.0833°, which is close to the spatial resolution of TROPOSIF product, and it was linearly interpolated and resampled to 0.05° to match the SIF dataset.

### 2.2.5. Selected pixels for typical PFTs

For the analysis of the relationship between GPP and SIF or NIRvP at the global scale, we focused on homogeneous pixels representative of broad vegetated plant functional types. We selected 150 representative pixels for each of 14 typical natural and agricultural plant functional types (PFTs) with a dominant PFT fraction >60% over selected 0.25° × 0.25° grid cells (150 homogeneous pixels for each PFT, listed in Table 1). The PFT map was derived from the merge of ESA CCI Land Cover (LC) products and LUH2 maps with a specific focus on the representation of crops (https://luh.umd.edu/data.shtml), and a LC-to-PFT cross-walking approach described by Poulter et al. (2015). For the detailed selection criteria of the pixels, please refer to Bacour et al. (2019).

**Table 1**
14 typical natural and agricultural plant functional types (PFTs) and the mean fraction of the dominant PFT over the selected 0.25° × 0.25° grid cells. 150 grid cells are selected per PFT (2100 in total).

| Abbreviation | Full name | Mean dominant PFT fraction |
|---|---|---|
| TrEBF | Tropical evergreen broadleaf forest | 0.95 |
| TrDBF | Tropical deciduous broadleaf forest | 0.69 |
| TeENF | Temperate evergreen needleleaf forest | 0.73 |
| TeEBF | Temperate evergreen broadleaf forest | 0.91 |
| TeDBF | Temperate deciduous broadleaf forest | 0.74 |
| BoENF | Boreal evergreen needleleaf forest | 0.71 |
| BoDBF | Boreal deciduous broadleaf forest | 0.69 |
| BoDNF | Boreal deciduous needleleaf forest | 0.62 |
| TeC3GRA | Temperate C3 grass | 0.94 |
| C4GRA | C4 grass | 0.95 |
| C3CRO | C3 crops | 0.87 |
| C4CRO | C4 crops | 0.77 |
| TrC3GRA | Tropical C3 grass | 0.96 |
| BoC3GRA | Boreal C3 grass | 0.98 |

### 2.2.6. Site scale in situ GPP and SIF dataset

The GPP data measured at five AmeriFlux sites with different PFTs were also used to evaluate the performance of the satellite based eSIF product for GPP estimation. As the spatial resolution of the satellite products used in this study is relatively low (0.05°), we only selected flux sites with homogeneous landcover to well match with the satellite observations. Using a 30 m landcover classification product (GLC-FCS30) (Zhang et al., 2021a), the fraction of dominant PFT in a 5 × 5 km$^2$ area) for each site was calculated, and only sites with dominant PFT fraction larger than 0.7 were used. The detailed information for five selected sites is shown in Table 2.

The tower-based synchronous SIF and GPP observations at two sites were also used to support the interpretation of the study results.

The first site is a cropland site located in the town of Xiao Tangshan (XTS; 116°27′E, 40°11′N) in the north of Beijing, China (temperate monsoon climate), with a yearly winter wheat and summer maize rotation; only data during the growing period of winter wheat from March to June in 2019 were used. The second site is an alpine grassland site located in the town of Arou (AR; 100°27′E, 38°02′N), China, in the middle reach of the Babao River Basin with an altitude of ~3000 m, which has a typical plateau continental climate; only data during the growing season (from June to September) in 2019 were used.

At both sites, a tower-based automatic SIF measurement system (Bergsun Inc., Beijing, China) was used to collect the canopy level downwelling and upwelling radiance spectra. The core of the system is an Ocean Optics QE65Pro spectrometer (Ocean Optics, Dunedin, Florida, USA) with a spectral resolution of ~0.34 nm and a signal-to-noise ratio of >1000. The systems used at the two sites were cross-calibrated before the beginning of operation in each year. For more details of the system, please refer to Du et al. (2019). The systems were amounted at a height of ~4 m and 17 m above the canopy at the XTS and AR sites, respectively. For both sites, the view zenith angle is 25°, and the view azimuth angle is ~210° (southwest). The field of view is 25°. The time interval for spectral data collection was ~3 min. SIF retrieval was conducted using the 3FLD method (Maier et al., 2003) at the $O_2$–A band, and was averaged using a 30 min window to reduce the noise. The canopy reflectance at 680 and 770 nm were used for the calculation of NIRv, and the downwelling irradiance at 770 nm was used as a proxy of PAR for the calculation of NIRvP.

Eddy covariance (EC) flux measurements were performed at both sites (Liu et al., 2011; Liu et al., 2018), and GPP data was calculated by carrying out gap filling and partitioning (daytime-based) processes using the online tool (http://www.bgc-jena.mpg.de/~MDIwork/eddyproc/) provided by the Max Planck Institute for Biogeochemistry (MPI-BGC) (Falge et al., 2001; Reichstein et al., 2005). The GPP data was also averaged using a 30 min window to match with the SIF dataset.

## 2.3. Data processing

### 2.3.1. Processing of the satellite dataset

According to Eq. (3), $\Phi_F$ can be estimated using SIF and NIRvP, and TOA radiance ($\mathrm{TOA_{Rad}}$) in the SIF retrieval fitting window is a good proxy for the product of PAR and near-infrared reflectance in the original NIRvP formulation (Dechant et al., 2020; Liu et al., 2020; Zeng et al., 2022a). Hence, the value of $\Phi_F$ for the TROPOSIF product was approximated as follows:

$$\Phi_F' = \frac{\mathrm{SIF_{TROPO}}}{\mathrm{NDVI_{MOD}} \times \mathrm{TOA_{Rad,TROPO}}} \tag{8}$$

The subscripts "TROPO" and "MOD" indicate that the parameters were from the TROPOSIF and MCD43C4 products, respectively. $\mathrm{SIF_{TROPO}}$ is the instantaneous SIF retrieved using the 743–758 nm spectral window (without daylength correction). The MCD43C4 product was resampled using the nearest neighbor method to match the pixels of

**Table 2**
Information for five selected AmeriFlux Sites.

| Site ID | Name | Latitude (°) | Longitude (°) | PFT | Dominant PFT fraction | Köppen climate zone* |
|---|---|---|---|---|---|---|
| US-CF1 | CAF-LTAR Cook East | 46.782 | −117.082 | Croplands (CRO) | 0.98 | Dsb |
| US-Var | Vaira Ranch- Ione | 38.413 | −120.951 | Grasslands (GRA) | 0.70 | Csa |
| US-Ton | Tonzi Ranch | 38.431 | −120.966 | Woody Savannas (WSA) | 0.74 | Csa |
| US-xSP | NEON Soaproot Saddle (SOAP) | 37.033 | −119.262 | Evergreen Needleleaf Forests (ENF) | 0.83 | Csa |
| US-xML | NEON Mountain Lake Biological Station (MLBS) | 37.378 | −80.525 | Deciduous Broadleaf Forests (DBF) | 0.78 | Dfb |

* Dsb: Mediterranean-influenced warm-summer humid continental climate; Csa: Hot-summer Mediterranean climate; Dfb: Warm-summer humid continental climate.

TROPOSIF L2B data. Here, we used "$\Phi_F{}'$" instead of "$\Phi_F$" in Eq. (8) to clarify their difference due to using $\text{TOA}_{\text{Rad}}$ instead of PAR × $\text{R}_{\text{NIR}}$, and the uncertainties in the NIRvP-based method to estimate $\Phi_F$. As introduced above, $\text{TOA}_{\text{Rad}}$ should have the same imaging geometry as SIF. Thus, the $\text{TOA}_{\text{Rad}}$ (averaged within 743–758 nm) from the TROPOSIF product was used. On the contrary, NDVI is expected to be more sensitive to atmospheric radiation transfer but less sensitive to directional effects (Sims et al., 2011; Zhang et al., 2016a; Zeng et al., 2022b); therefore, NDVI was calculated using the MODIS nadir BRDF-adjusted reflectance in the MCD43C4 product.

Second, the median of $\Phi_F{}'$ in 8 days was calculated for each 0.05° grid cell to reduce the influence of outliers. Moreover, a gaussian-weighted moving average filter with a window size of 5 × 5 pixels (0.25° × 0.25°) was used to smooth $\Phi_F{}'$ to reduce the influence of noise and missing values (see Section 4.4 for the discussion on the window size). $\Phi_F{}'$ values smaller than −0.02 and larger than 0.05 (determined approximately using 1.5 times the interquartile range) were regarded as outliers.

Finally, the enhanced SIF product (eSIF), combining the information of NIRv and PAR at a spatial resolution of 0.05° and a temporal resolution of 8 days, was calculated as follows:

$$\text{eSIF} = \overline{\text{PAR}}_{\text{ERA5}} \times \text{NIRv}_{\text{MOD}} \times \overline{\Phi_F'} \quad (9)$$

where $\overline{\text{PAR}}_{\text{ERA5}}$ is the 8-day averaged PAR derived from the ERA5 shortwave radiation, $\text{NIRv}_{\text{MOD}}$ is the NIRv calculated using the MODIS nadir BRDF-adjusted reflectance with a time step of 8 days, and $\overline{\Phi_F'}$ is the smoothed $\Phi_F{}'$ using the gaussian-weighted moving average filter. Using the averaged PAR from the ERA5 dataset, instantaneous SIF data can be converted into 8-day composites to better match the FLUXCOM GPP product for evaluation. The nadir BRDF-adjusted reflectance from MODIS was used to reduce the directional effect in SIF retrieval.

For comparison, the 8-day averaged NIRvP ($\overline{\text{PAR}}_{\text{ERA5}} \times \text{NIRv}_{\text{MOD}}$) (Fig. 3, left panels) and the 8-day averaged original TROPOMI SIF (Fig. 3, right panels) with spatial resolution of 0.05° were also calculated.

### 2.3.2. Processing of the in situ dataset

The site dataset was processed using a similar theoretical framework to that described in Section 2.1. However, the smoothing of $\Phi_F$ was performed temporally (rather than spatially as for the space-borne data) using a gaussian-weighted moving average window with a size of 20 samples (which is approximately the number of samples within one day). The view angles for the spectral measurements were fixed and the influence of the diurnal variation of the sun illumination angle (which is relatively small, see discussion in Section 4.4) was ignored in this study (same as for the satellite dataset). Therefore, we did not perform any directional normalization of NIRv. Moreover, as both the SIF and GPP datasets were acquired concomitantly every 30 min and can match with each other, the temporal upscaling of PAR was not required. In summary, $\Phi_F{}'$ and eSIF for site dataset were calculated using Eq. (10) and Eq. (11),

$$\Phi'_{F,\text{site}} = \frac{\text{SIF}_{\text{Canopy}}}{\text{NDVI} \times \text{Rad}_{\text{NIR,TOC}}} \quad (10)$$

$$\text{eSIF}_{\text{site}} = \text{NDVI} \times \text{Rad}_{\text{NIR,TOC}} \times \overline{\Phi'_{F,\text{site}}} \quad (11)$$

where $\text{SIF}_{\text{Canopy}}$ is the 760 nm SIF retrieved at canopy level, NDVI is calculated using the measured top-of-canopy (TOC) reflectance, $\text{Rad}_{\text{NIR,TOC}}$ is the upwelling near-infrared radiance at TOC, and $\overline{\Phi'_{F,\text{site}}}$ is the smoothed $\Phi_{F,\text{ site}}{}'$ in the temporal dimension.

## 3. Results

### 3.1. Relationships of eSIF with NIRvP and SIF

Fig. 2 shows the global eSIF map averaged over 28 July to 4 August 2019 at a 0.05° spatial resolution, and Fig. 3 shows the regional zoom-ins of NIRvP ($\overline{\text{PAR}}_{\text{8d,ERA5}} \times \overline{\text{NIRv}}_{\text{8d,MOD}}$), eSIF, and SIF (simply averaged using instantaneous values from the TROPOSIF baseline product) in the Yangtze River, Mississippi River, and Nile River regions. It can be seen that the eSIF has smooth spatial varriations as for NIRvP and less patchy structures (associated to retrieval errors) than SIF. On another hand, the spatial patterns of eSIF are more similar to those of SIF than to NIRvP (see their radial and zonal distribution profiles in Fig. S1). Moreover, the smoothness of $\Phi_F$ instead of SIF could better preserve the spatial texture features, as the high spatial resolution of NIRvP was kept (see Fig. S2).

As expected, the results show that the eSIF product is less noisy than SIF, and preserves the unique physiology-related characteristics of SIF. In other words, eSIF shows unique advantages compared to both SIF and NIRvP.

Further, the temporal and spatial correlations of eSIF with NIRvP and SIF were analyzed quantitatively at global scale, as shown in Fig. 4. For most vegetated areas, eSIF shows strong linear correlations with both NIRvP and SIF (with $\text{R}^2 > 0.7$), and the $\text{R}^2$ for the temporal correlation of eSIF with NIRvP is higher than that for the correlation of eSIF with SIF in general (possibly due to the relatively large noise in original SIF data). For the spatial correlations, the medians of $\text{R}^2$ for eSIF-NIRvP and eSIF-SIF correlations are similar (∼ 0.8), but annual variation range of $\text{R}^2$ for eSIF-NIRvP correlation is larger than that for eSIF-SIF correlation, which indicates a more stable relationship through the year.

### 3.2. Relationships of NIRvP, eSIF and SIF with GPP

#### 3.2.1. Correlations with FLUXCOM GPP at global scale

To evaluate the potential of eSIF for estimating GPP, firstly, we compared the $\text{R}^2$ for the temporal correlations of eSIF, NIRvP, and SIF with FLUXCOM GPP at global scale for the year 2019, as shown in Fig. 5. Both NIRvP and eSIF show strong temporal correlations with GPP for most vegetated areas with $\text{R}^2 > 0.7$, while the temporal correlation of SIF with GPP is relatively weaker. As shown in Fig. 5 (d), eSIF shows stronger temporal correlation with GPP than NIRvP at regions of central America, Mediterranean basin, central Africa, south Asia and the coast of Australia, which are mainly regions with tropical and Mediterranean

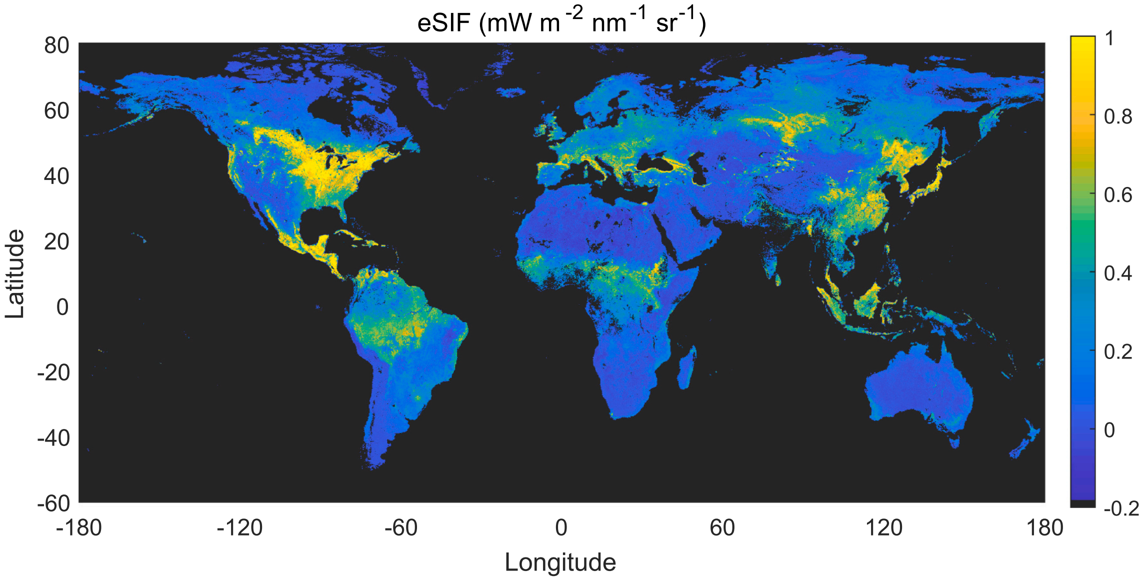

**Fig. 2.** Global composite of eSIF over 8 days (28 July to 4 August 2019) at a 0.05° spatial resolution.

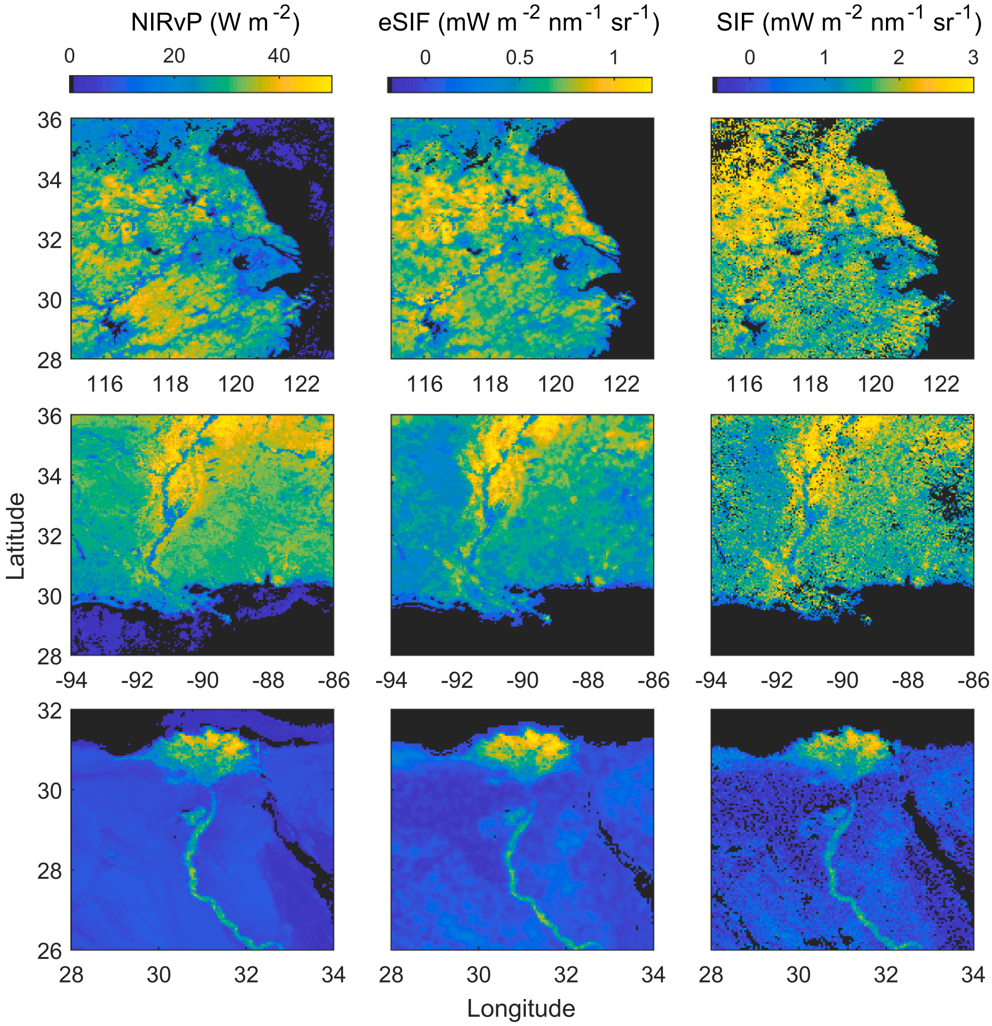

**Fig. 3.** Spatial patterns of NIRvP (left), eSIF (middle), and SIF (right) in the Yangtze River (top), Mississippi River (middle), and Nile River (bottom) regions averaged over 28 July to 4 August 2019, at 0.05° resolution. NIRvP was calculated using ERA5 shortwave radiation and MODIS nadir BRDF-adjusted reflectance, and SIF was from the original TROPOMI SIF retrievals (simply averaged using instantaneous values from the TROPOSIF baseline product). The spatial resolution was 0.05°.

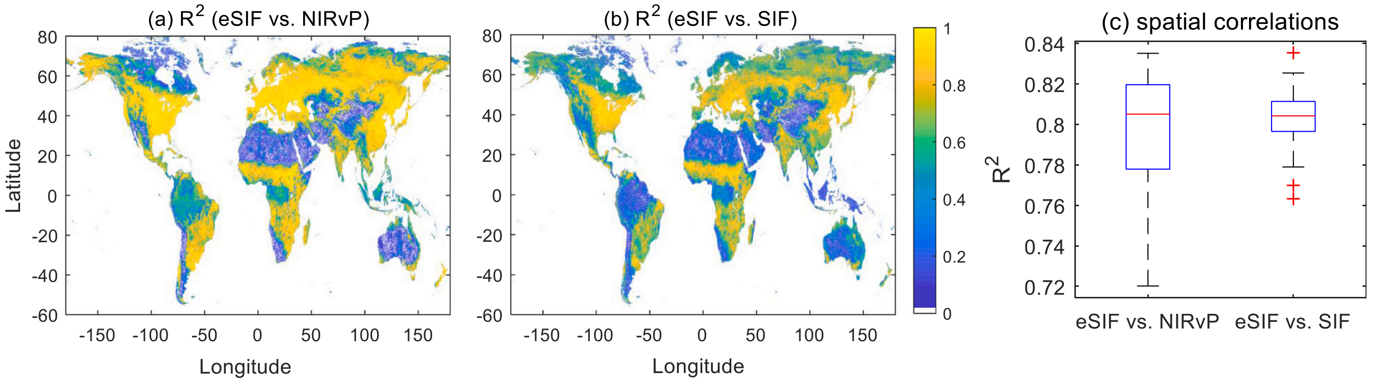

**Fig. 4.** The coefficient of determination ($R^2$) for temporal (a, b) and spatial (c) correlations (linear models) of eSIF with NIRvP and SIF at global scale for the year 2019. The boxplot in (c) shows the annual distribution of $R^2$ for the global spatial correlations. The bottom and top of each box represent the first and third quartiles, respectively, the red lines in the boxes show the medians, the whiskers show the maximum/minimum values within 1.5 times the interquartile range, and the red crosses show the outliers. (For interpretation of the references to colour in this figure legend, the reader is referred to the web version of this article.)

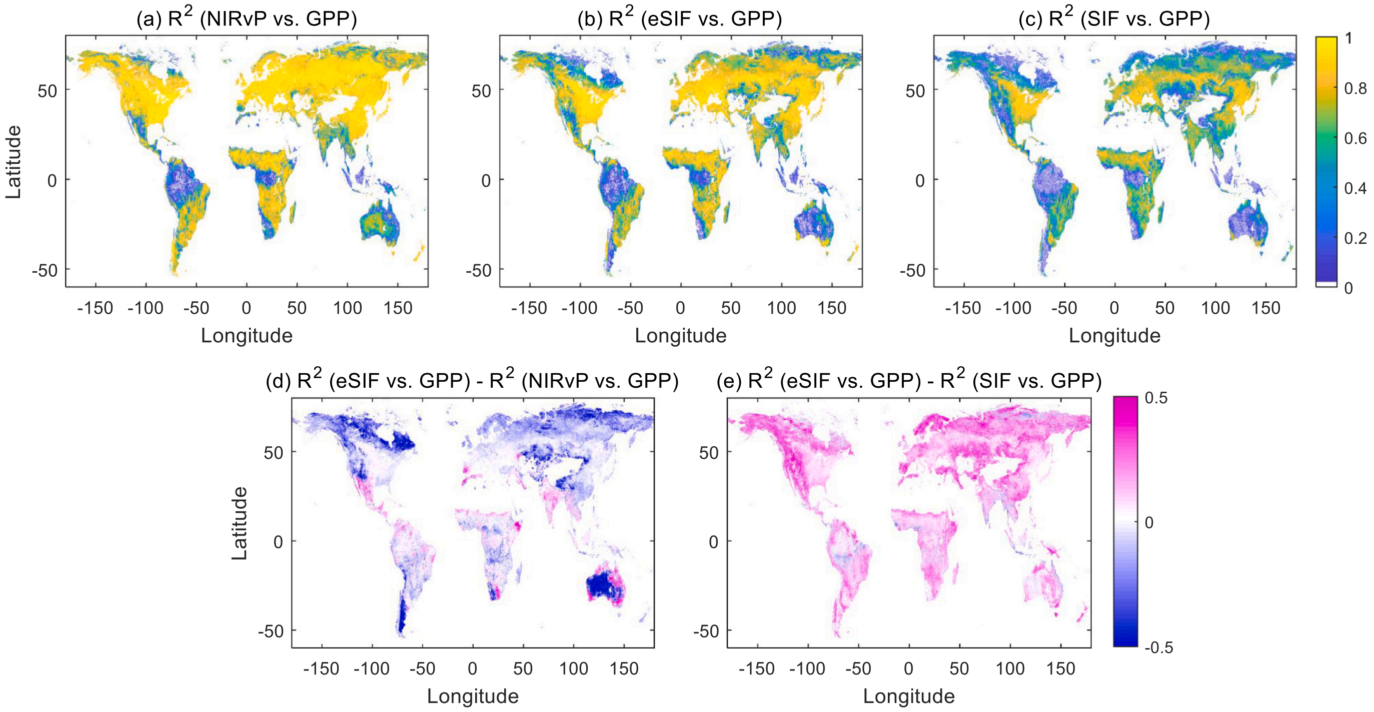

**Fig. 5.** $R^2$ for temporal correlations (linear models) of NIRvP (a), eSIF (b) and SIF (c) with FLUXCOM GPP and their differences (d, e) at global scale for the year 2019.

climates, and the annual pattern of radiation or temperature is usually different with that of precipitation; while at most of other areas, NIRvP shows stronger temporal correlation with GPP than eSIF. As shown in Fig. 5 (e), eSIF outperformed SIF in the temporal correlation with GPP for almost all pixels.

### 3.2.2. *Correlations with FLUXCOM GPP for different PFTs*

Focusing on different PFTs, we compared the relationships of NIRvP, eSIF, and SIF with FLUXCOM GPP for the year 2019 for various PFTs, using all selected pixels introduced in Section 2.2.5. As distinct SIF–GPP relationships between woody and herbaceous vegetation has been reported (Pickering et al., 2022), we grouped the PFTs into forest and grass/crop types. In general, all three variables show strong correlations with GPP. The relationships for grass and crop PFTs were found more linear than those for forest PFTs. Therefore, both nonlinear (using a rational function in the form of $y = (p_1x + p_2)/(x + q)$) (Damm et al., 2015) and linear regression performances were tested for forest PFTs, while only linear regression performances were tested for the grass/crop PFTs.

As shown in Fig. 6, for both forest and grass/crop PFTs, eSIF outperformed SIF for GPP estimation, with the $R^2$ increasing from 0.60 to 0.68 for forest PFTs, and from 0.67 to 0.74 for grass/crop PFTs. The main patterns of the eSIF–GPP and SIF–GPP relationships were similar, but the dispersion was lower for eSIF–GPP, which indicates that the noise in SIF was efficiently reduced, while the key information was preserved.

For forest PFTs, NIRvP showed the strongest correlation with GPP, with a nonlinear regression determination coefficient ($R^2$) of 0.80 (linear regression $R^2$ of 0.77), and the relationship of NIRvP with GPP was more linear than that of eSIF with GPP; while for grass/crop PFTs, eSIF outperformed NIRvP, with an $R^2$ of 0.74 for eSIF and 0.65 for NIRvP.

Further, the spatial and temporal correlations were analyzed separately, as shown in Fig. 7. For both spatial and temporal correlations,

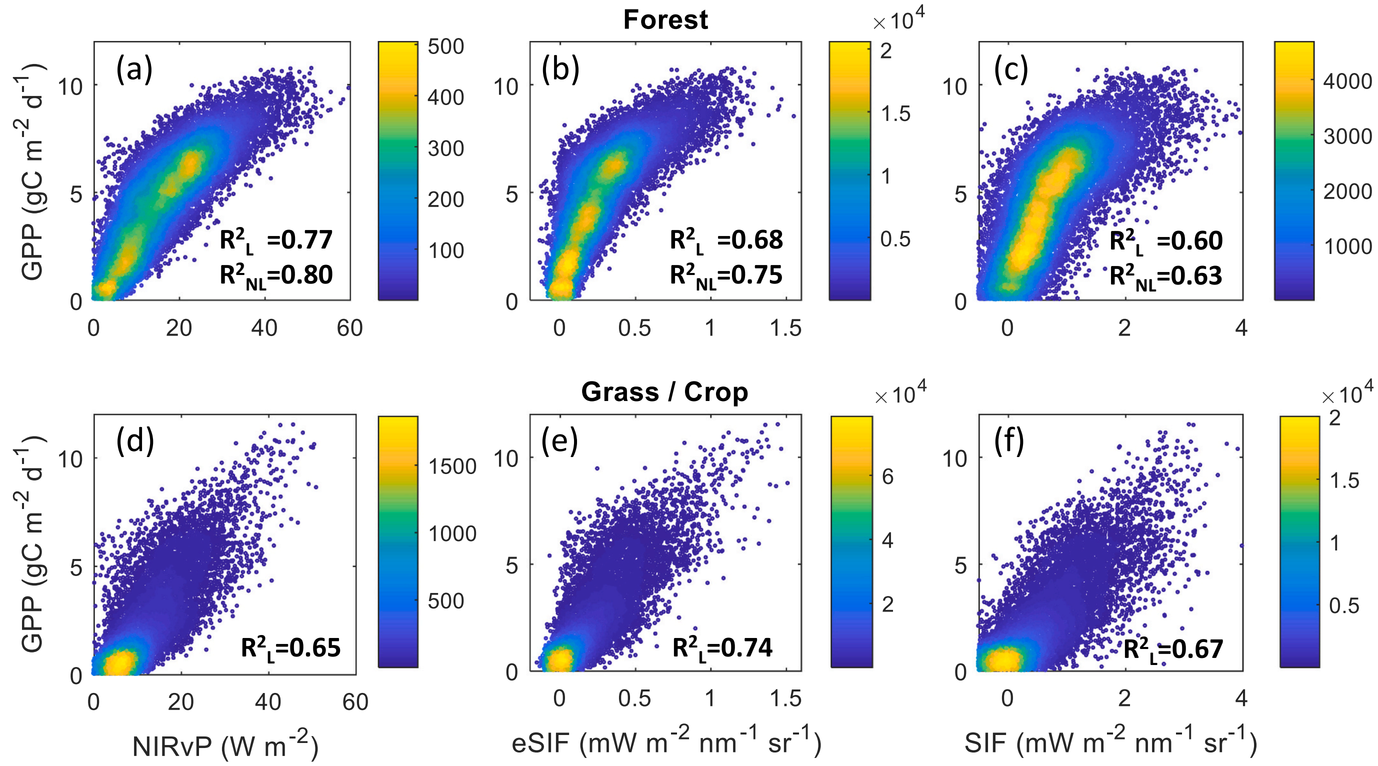

**Fig. 6.** Spatio-temporal correlations between NIRvP, eSIF, and SIF with FLUXCOM GPP for all of the selected pixels of typical PFTs for 2019. The 14 typical PFTs are separated into two groups (forest and grass/crops). The determination coefficients for linear regressions ($R^2_L$) and nonlinear regression ($R^2_{NL}$) are shown in each panel. The colorbars correspond to the point density (bin count).

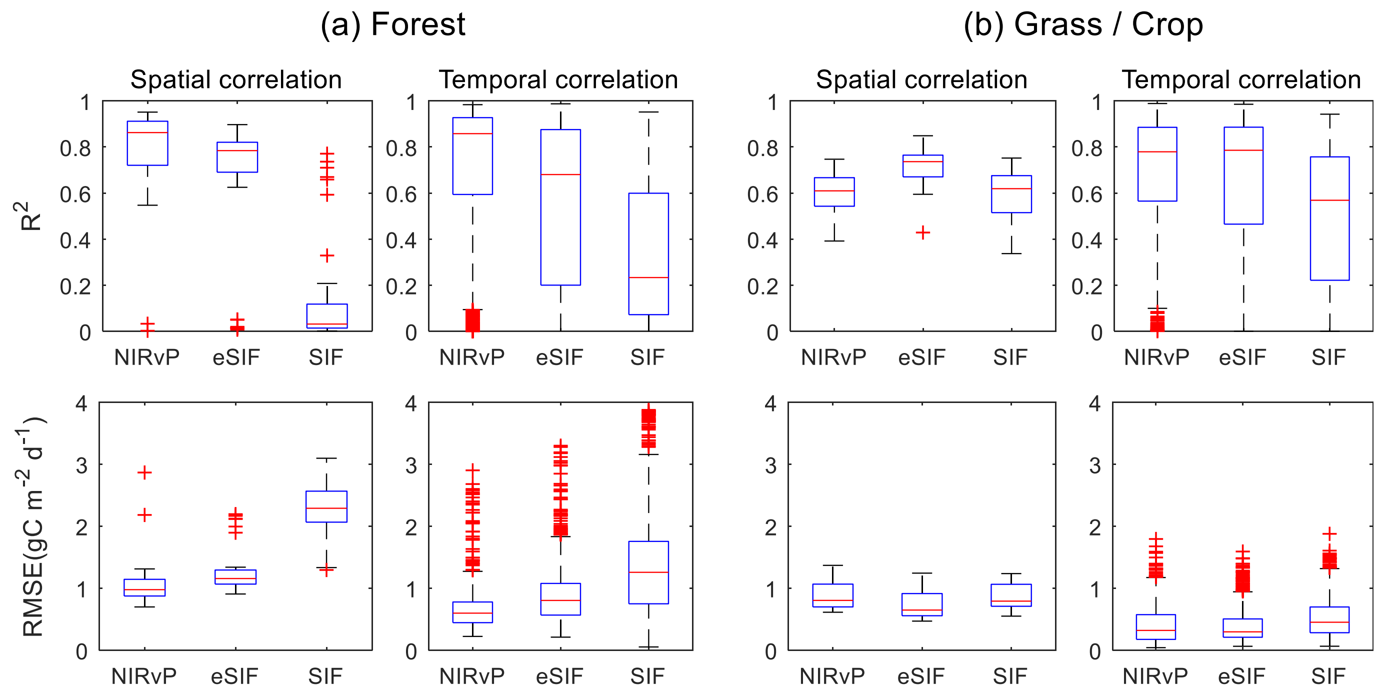

**Fig. 7.** $R^2$ and root mean squared error (RMSE) for spatial and temporal correlations of NIRvP, eSIF and SIF with GPP for forest (a, nonlinear model) and grass/crop (b, linear model) PFTs for the year 2019. For spatial correlations, the boxplots show the annual distribution of $R^2$ and RMSE; for temporal correlations, the boxplots show the distribution of $R^2$ and RMSE across pixels.

NIRvP performs best for forest PFTs, while eSIF performs best for grass/crop PFTs. And the better performance of eSIF for grass/crop PFTs is clearer for the spatial than temporal correlation.

### 3.2.3. *Correlations with in situ GPP at site scale*

The correlations of NIRvP, eSIF and SIF with GPP were also compared using in situ GPP data in 2019 from five AmeriFlux sites in with different PFTs introduced in Section 2.2.6, as shown in Fig. 8 and

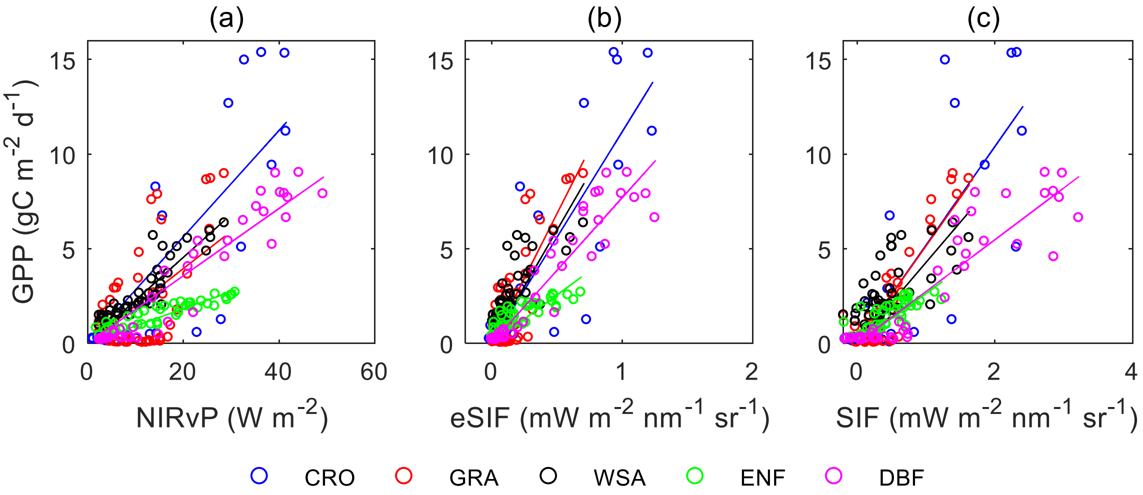

**Fig. 8.** Relationships of NIRvP, eSIF, and SIF with GPP at five AmeriFlux sites for different PFTs in 2019.

**Table 3**
$R^2$ for the linear correlations of NIRvP, eSIF, and SIF with GPP at five AmeriFlux sites for different PFTs in 2019. The maximum of $R^2$ in each row is marked using bold font.

| PFT (Site) | NIRvP | eSIF | SIF |
|---|---|---|---|
| CRO (US-CF1) | 0.71 | **0.74** | 0.66 |
| GRA (US-Var) | 0.34 | 0.65 | **0.82** |
| WSA (US-Ton) | **0.81** | 0.63 | 0.46 |
| ENF (US-xSP) | **0.85** | 0.72 | 0.51 |
| DBF (US-xML) | **0.93** | 0.90 | 0.85 |
| All | 0.57 | **0.66** | 0.59 |

Table 3. At the CRO site, eSIF performs best for GPP estimation and followed by NIRvP; at the GRA site, SIF performs best and followed by eSIF, while the $R^2$ for NIRvP-SIF correlation is only 0.34 (the possible reason is discussed in Section 4.1); at the WSA, ENF and DBF sites, NIRvP performs best for GPP estimation. When pooling data at all five sites, eSIF outperforms both NIRvP and SIF for GPP estimation. These results are consistent with the results from FLUXCOM GPP, which indicate that NIRvP may have more potential for GPP estimation for forest PFTs, while eSIF may have more potential for GPP estimation for grass and crop PFTs. Moreover, eSIF may have more universal correlation with GPP across different PFTs.

### *3.3. Variation in the ratios of GPP to NIRvP and eSIF across PFTs*

The PFT-dependency is a major uncertainty for GPP estimations models. In this part, therefore, we investigated the potential of eSIF to represent varying LUE across PFTs, using both global satellite and canopy level site datasets.

#### *3.3.1. Global satellite dataset*

Fig. 9 shows the ratios (calculated as the slopes of the linear regression without intercept) of GPP to NIRvP (a) and eSIF (b) for different PFTs. Moreover, the coefficients of variation (CVs) for the ratios of GPP to NIRvP and eSIF across different PFTs are shown in Table 4.

For forest PFTs, the CVs for the ratios of GPP to eSIF were higher than that for the ratios of GPP to NIRvP. The ratio for BoENF was considerably higher than that for other PFTs for both NIRvP and eSIF, but much higher for eSIF. When excluding BoENF, the CVs for the ratios of GPP to NIRvP and eSIF for forest PFTs were both smaller than 10%.

For grass/crop PFTs, the CV for the ratios of GPP to eSIF (18.9%) was smaller than that for the slope of GPP to NIRvP (27.3%). The ratios of GPP to eSIF for C4 grass and crops were higher than that for C3 grass and crops. However, the ratio of GPP to NIRvP for C4 crops was slightly

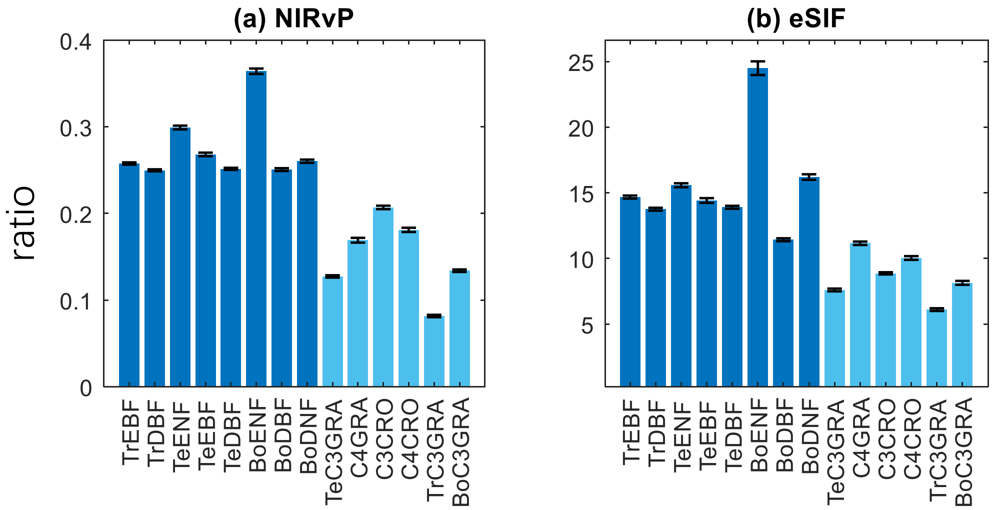

**Fig. 9.** The ratios (calculated as the slopes of the linear regression without intercept) of GPP to NIRvP (a) and eSIF (b) for different PFTs. The errorbar shows the 95% confidence bounds of the linear regression. The dark blue bars represent forest PFTs, and the light blue bars represent grass/crop PFTs. (For interpretation of the references to colour in this figure legend, the reader is referred to the web version of this article.)

**Table 4**
Coefficients of variation (CV) for the ratios of GPP to NIRvP and eSIF across different PFTs.

| PFT groups | NIRvP | eSIF |
|---|---|---|
| All PFTs | 33.0% | 35.8% |
| Forest PFTs | 13.4% | 23.3% |
| Forest PFTs except BoENF | 6.2% | 9.9% |
| Grass/crop PFTs | 27.3% | 18.9% |
| C3 Grass/crop PFTs | 32.7% | 13.2% |

lower than that for C3 crops. When excluding C4 PFTs, the CV for the ratios of GPP to eSIF (13.2%) was much smaller than that for the slope of GPP to NIRvP (32.7%). These results indicate that eSIF would have more potential to represent the variation in the light use efficiencies for grass and crop PFTs, while NIRvP may have more potential for forest PFTs.

Specifically, as shown in Fig. 10, C3CRO and TeC3GRA are selected as cases to show the different performances of NIRvP and eSIF for estimating GPP, and the performance of original SIF is also shown for comparison. The slope (ratio) of GPP to NIRvP for C3CRO is considerably higher than that for TeC3GRA. On the contrary, the slope of GPP to eSIF for C3CRO is very close to that for TeC3GRA. The slope of GPP to original SIF for C3CRO is also higher than that for TeC3GRA, but the difference is smaller than that of GPP to NIRvP. When put data of the two PFTs together, the $R^2$ for the relationship of eSIF with GPP is the highest.

### *3.3.2. Site scale in situ dataset*

The site dataset was also used to confirm the results from the satellite dataset. Similarly to Fig. 10, Fig. 11 shows that the slope (ratio) of GPP to NIRvP for winter wheat at the XTS site was considerably higher than that for alpine grassland at the AR site. On the contrary, the slopes of GPP to eSIF and SIF for winter wheat were very close to that for alpine grassland. And when pooling the data of winter wheat and grass, the $R^2$ for the relationship of eSIF with GPP is the highest. Although the NIRvP showed less scatter and more linear correlation with GPP for single PFT, eSIF showed more potential to unify the GPP estimation models for grass and crops. It needs to be noted that, the satellite datasets are with temporal resolution of 8 days, and represent the seasonal variation of NIRv, eSIF, SIF and GPP; while the in situ datasets are with temporal resolution of 30 min, and can represent both diurnal and seasonal variation of the parameters.

### *3.4. Seasonal patterns of GPP, eSIF, and NIRvP*

To verify that eSIF conveys more physiological information on plant PFTs than NIRvP (e.g., was more sensitive to environmental stress), we compared the seasonal patterns of GPP, eSIF, and NIRvP, together with environmental parameters, including air temperature (Tair), VPD, and PAR from ERA5 dataset. BoENF in the Northern Hemisphere and TrC3GRA in the Southern Hemisphere were selected as test cases, as these PFTs usually suffer from cold or dry conditions, respectively, in specific seasons. The locations of the selected pixels are shown in Fig. S3, and the scatter plots for the NIRvP/eSIF vs. GPP relationships are shown in Fig. S4.

BoENF is mainly distributed in North America and Eurasia. The large variation in temperature through the year is the main environmental factor influencing the activity of photosynthesis. As shown in Fig. 12(a), when DOY <70 (before mid-March), $T_{air}$ was below 0 °C. During this period, both GPP and eSIF were close to 0 and were relatively stable, which indicates that photosynthesis was strongly limited by the low temperature. However, NIRvP increased continuously with an increasing PAR, because the canopy structure of evergreen forests was relatively stable throughout the year.

TrC3GRA is mainly distributed in the tropical and subtropical areas in Africa and Australia. We only used pixels in the Southern Hemisphere in order to avoid any influence of the opposite season in Northern and Southern Hemispheres. For TrC3GRA, $T_{air}$ remained at a high level throughout the year. PAR was relatively low in the middle of the year and high at the beginning and end of the year due to the variation of solar zenith angle, but also remained at a high level (>60 W $m^{-2}$) throughout the year. VPD varied with the altering of dry and wet seasons, with a relatively low value in the middle of the year. Water stress was then the main factor limiting the photosynthesis for TrC3GRA. As shown in Fig. 12(b), both GPP and eSIF increases in the first half of the year and decreases in the latter half, with a high value in the middle of the year (corresponding to the wet season), but NIRvP and PAR showed inverse seasonal patterns, with a low value in the middle of the year.

To sum up, these results show that, compared to NIRvP, eSIF can better track the influence of environmental factors (e.g., low temperature on BoENF and water stress on TrC3GRA) on GPP, which indicates that eSIF contains more physiological information than NIRvP.

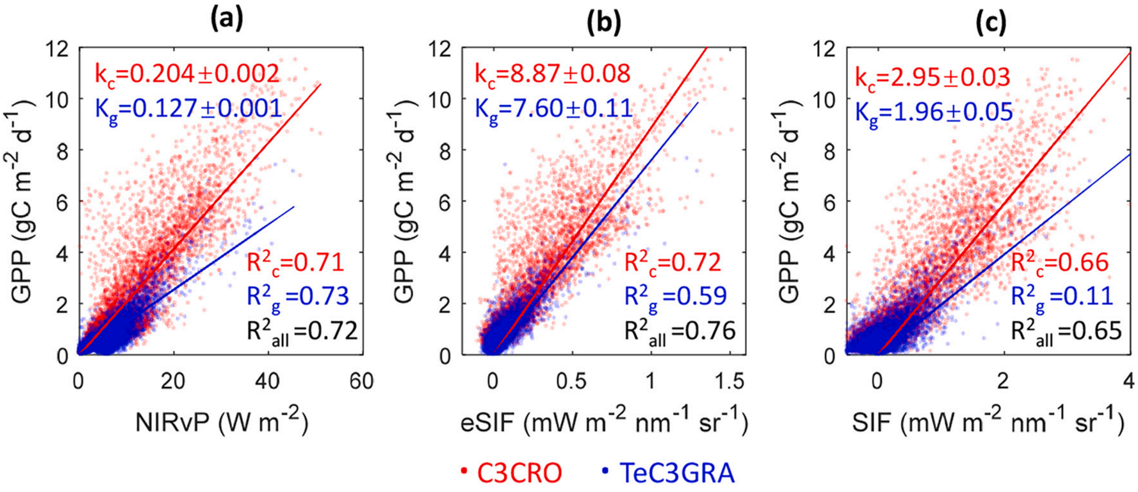

**Fig. 10.** Comparison of the correlations of NIRvP (a), eSIF (b) and SIF (c) with GPP for C3CRO (red) and TeC3GRA (blue) in 2019. The solid lines show the linear regression results without intercept. k is the regression slope (ratio) with 95% confidence intervals, and $R^2$ is the coefficient of determination, and the subscripts "c", "g", "all" represent data of C3CRO, TeC3GRA and all together, respectively. (For interpretation of the references to colour in this figure legend, the reader is referred to the web version of this article.)

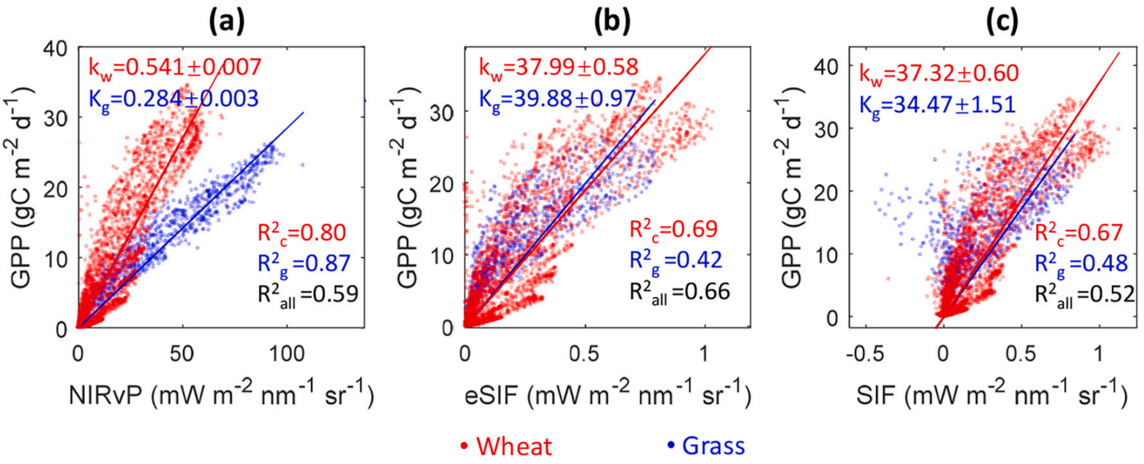

**Fig. 11.** Comparison of the correlations of NIRvP (a), eSIF (b) and SIF (c) with GPP for winter wheat at the XTS site (red) and alpine grassland at the AR site (blue) in 2019. The solid lines show the linear regression results without intercept. k is the regression slope (ratio) with 95% confidence intervals, and $R^2$ is the coefficient of determination, and the subscripts "w", "g", "all" represent data of wheat, grass and all together, respectively. (For interpretation of the references to colour in this figure legend, the reader is referred to the web version of this article.)

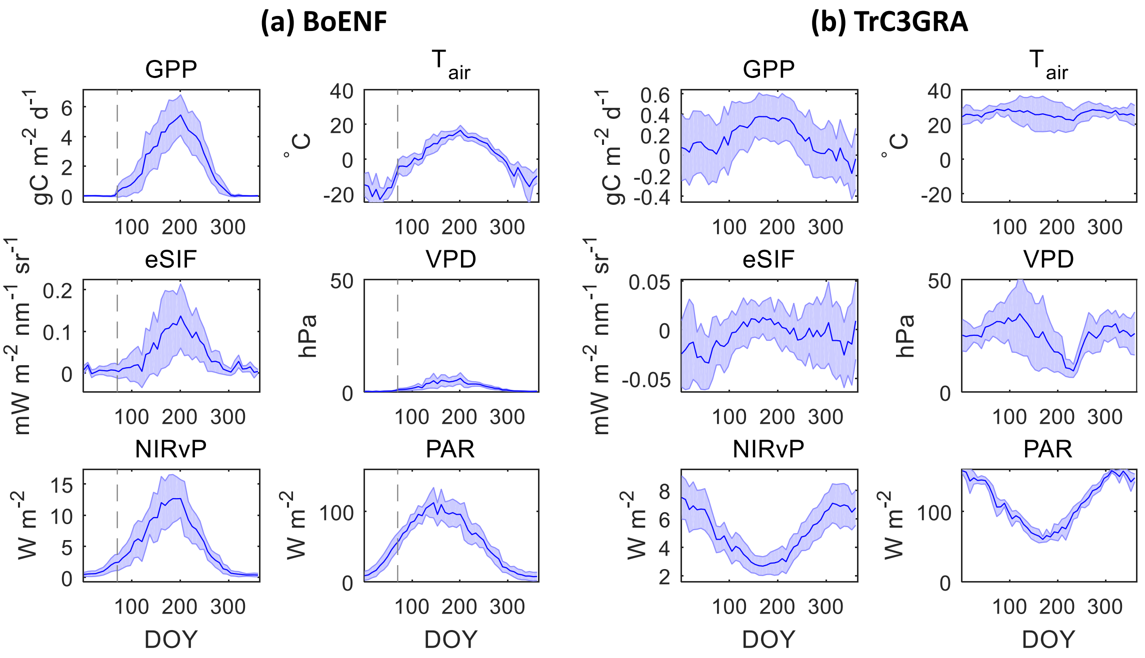

**Fig. 12.** Seasonal patterns of GPP, eSIF, NIRvP, air temperature ($T_{air}$), VPD, and PAR for BoENF in the Northern Hemisphere (a) and TrC3GRA in the Southern Hemisphere in 2019. The solid line represents the mean values for different pixels, and the shade represents the standard deviations. The grey dashed line in (a) marks the DOY 70.

## 4. Discussion

### 4.1. Complementarity of the optical and physiological components of SIF

According to Eq. (3), near-infrared SIF can be approximated as the product of NIRvP and $\Phi_F$. NIRvP has been regarded as a structural proxy of SIF (Dechant et al., 2020; Dechant et al., 2022; Zeng et al., 2022b). We prefer to define NIRvP as the "optical component" of SIF because it is determined by several optical parameters, including incident radiation (PAR) and canopy absorption and scattering ($f$APAR and $f_{esc}$), and it is not only determined by canopy structure, but also by leaf pigments (nevertheless, leaf pigments only played a minor role compared to canopy structure (Asner and Wessman, 1997; Asner, 1998; Luo et al., 2019; van der Tol et al., 2019)). On the contrary, $\Phi_F$ is mainly related to the physiological status of vegetation, and has been defined as the "physiological component" of SIF (Dechant et al., 2022; Dechant et al., 2020). $\Phi_F$ is a unique characteristic of SIF compared to the traditional reflectance-based vegetation indices, which makes it the "essence" of SIF. The results of this study and those of previous works (Dechant et al., 2022; Dechant et al., 2020; Yang et al., 2021; Zeng et al., 2022a) have shown that NIRvP and $\Phi_F$ considerably have different characteristics, and would have complementarity contributions to GPP monitoring.

Several recent studies have reported the good performance of NIRvP for GPP estimation (Baldocchi et al., 2020; Dechant et al., 2022; Dechant et al., 2020; Liu et al., 2020; Wu et al., 2020). The mechanism behind the correlation of NIRvP and GPP is that, for non-stressed situations, both of them are dominated by APAR, and that $f_{esc}$ (or NIRv/$f$APAR) has similar diurnal and seasonal patterns with LUE for specific species (Dechant et al., 2020; Liu et al., 2020). Both $f_{esc}$ and LUE are highly related to canopy structure and the illuminating condition (e.g., the diffuse radiation ratio) (Gu et al., 2002; Kim et al., 2021). Therefore, although $f_{esc}$ and LUE are structural and functional traits of vegetation, respectively, they are "indirectly" correlated to each other, especially in temporal dimension and no-stressed situations. Moreover, the high data quality of NIRvP also guarantees its strong correlation with GPP.

However, previous studies have also shown that NIRvP is unable to satisfactorily track the decrease in GPP for BoENF in winter, as the canopy structure and APAR did not significantly change, while the light use efficiency apparently decreased in winter (Magney et al., 2019). Our results confirmed the fact that NIRvP is unable to monitor the variation in GPP under some environmental conditions, such as low temperature for BoENF in winter and water stress for TrC3GRA in the dry season, as shown in Fig. 12.

In contrast, the physiological component of SIF, $\Phi_F$, is more directly related to the photosynthesis process. $\Phi_F$ and the photochemical quantum yield of photosystem II ($\Phi_{PSII}$) are determined by the first-order rate constants of several energy pathways, including fluorescence emission, non-photochemical quenching, photochemical quenching, and constitutive thermal dissipation (Frankenberg and Berry, 2018; Porcar-Castell et al., 2014). As introduced by Gu et al. (2019), $\Phi_F$ can directly track some of the variation in $\Phi_{PSII}$ due to the change of vegetation physiological status, which is the basis to establish a mechanistic model for SIF-based GPP estimation.

However, the relationship between $\Phi_F$ and LUE is still complex and unclear. Besides photosynthesis (or photochemical quenching (PQ)) and chlorophyll fluorescence, non-photochemical quenching (NPQ) in forms of heat dissipation is another way for energy partitioning in PSII (Porcar-Castell et al., 2014, 2021). So the variation of NPQ is a large uncertainty in the relationship of $\Phi_F$ and LUE. The influence of environmental factors on the relationship of $\Phi_F$ and LUE have been reported (e.g. Wohlfahrt et al., 2018; Martini et al., 2022; Liu et al., 2021).

The results of this study show the ability of eSIF (NIRvP × $\Phi_F$) to track the variation in GPP for BoENF and TrC3GRA at cold or dry conditions (Fig. 12). These results are consistent with those reported by Magney et al. (2019), which shows that SIF can track the decrease in GPP for BoENF in winter, when NIRvP is inefficient. Moreover, Dechant et al. (2022) showed that the ratio of SIF to NIRvP (i.e., $\Phi_F$) has notable seasonal variation for different ecosystems; Zeng et al. (2022a) also showed that $\Phi_F$ can detect several effects of abiotic changes, such as heat stress; Turner et al. (2021) showed that SIF can better track decreases in GPP due to extreme drought than NIRv, suggesting that SIF is a measure of photosynthetic activity as opposed to photosynthetic capacity. In addition, Khan et al. (2022) suggested to use a non-linear light response curve to fit the NIRvP-GPP relationship for Oak Savanna ecosystem to deal with the light saturation of GPP. These related works confirm the results of this study.

Another advantage of SIF and eSIF over NIRvP for tracking GPP is their smaller scale effect. As Table 3 shows, SIF and eSIF largely outperformed NIRvP for tracking GPP at the GRA site (US-Var). The $R^2$ values for the SIF, eSIF, or NIRvP vs. GPP relationship are 0.82, 0.65 and 0.34, respectively. The results seem contradictory to that of Baldocchi et al. (2020), in which much better NIRvP-GPP relationship ($R^2 = 0.80$) for the same site was reported. The NIRvP in Baldocchi et al. (2020) was calculated using in situ measurements, which could nicely match with the in situ GPP. But the NIRvP in this study was from MODIS product with 0.05° spatial resolution. To find out the reason, the annual variations of NDVI, $R_{NIR}$, PAR, NIRvP, eSIF, SIF and GPP at the site with spatial resolution of 0.05° were analyzed (Fig. S5). After June, although NDVI decreases largely, it is still higher than 0.35. Meanwhile, both $R_{NIR}$ and PAR stay at high level. These reasons make the decrease of NIRvP is much smaller than that of GPP after June, and result in the weak relationship between NIRvP and GPP. In the 0.05° pixel, the landcover contains not only grass, but also trees, and the flux site locates at the edge of the MODIS pixel with a smaller footprint (Fig. S6). Kong et al. (2022) pointed out that the robust NIRvP-GPP relationship relies on their matched footprints. Furthermore, the climate type for US-Var site is Mediterranean. In the hot and dry summer, the grass turns to brown while the trees stay green. Although the fraction of grass within 5 × 5 $km^2$ region is as high as ~70%, the green tree will make large contribution to the NDVI, due to the large scale effect of NDVI (Zeng et al., 2022b). On the contrary, as an emitted signal, SIF, in principle, would not suffer from scale effect. Therefore, SIF and eSIF are less influenced by the trees in the pixel, and better track the decrease of grass GPP in the dry season, as shown in Fig. S5. And the better performance of SIF than eSIF may partly related to the uncertainties in estimation of $f_{esc}$ for sparse vegetation (see Section 4.5).

One more thing to be noted is, in this study, we used SIF/NIRvP (Zeng et al., 2022a) to estimate $\Phi_F$ (the symbol "$\Phi_F{}'$" was used to clarify its difference from "real" $\Phi_F$ in this study). But the method has been found not so accurate for sparse vegetations (Joiner and Yoshida, 2020; Wieneke et al., 2018; Jonard et al., 2020). This fact would introduce some uncertainties to the analysis on the physiological component of SIF, but it has little influence on the calculation of eSIF, because $\Phi_F$ or $\Phi_F{}'$ only serves as an intermediate variable. Therefore, the analysis on physiological component of SIF in this study is mainly based on the comparison between eSIF and NIRvP, rather than directly using $\Phi_F{}'$. Recently, some refinements have been made to NIRv, such as NIRv from hyperspectral measurement (NIRvH) proposed by Zeng et al. (2021) and soil-adjusted NIRv (SANIRv) proposed by Jiang et al. (2021) to minimize the impact of soil. These refinements may help to improve the estimation of $f_{esc}$ in future.

### *4.2. The PFT-dependency for relationships of NIRvP and eSIF with GPP*

Both NIRvP and eSIF showed PFT-dependent relationship with GPP, especially between forests and grass/crop PFTs.

Among grass/crop PFTs, the variation in the regression slopes of the eSIF–GPP relationship was smaller than that of the NIRvP–GPP relationship (Figs. 9 - 11 and Table 4), which indicates that $\Phi_F$ has the potential to represent the differences in LUE across grass/crop PFTs. The difference in the slopes of NIRvP-GPP relationship for grass and crop was not reported in some relevant studies, such as Jiang et al. (2021) and Badgley et al. (2019), in which only used different slopes for C3/C4 plants, and for deciduous/evergreen forests. From Fig. 10(a), we can see that the difference in slopes of NIRvP-GPP relationship for grass and crop PFTs is relatively small at global scale (the $R^2$ is similar for separated and combined models). But the difference is much larger for site scale data, as shown in Fig. 11(a). The grass site (AR) used in Fig. 11 is an alpine grassland site located at the Qinghai-Tibet Plateau, and its much harsher climate than that for the wheat site (XTS) located at the North China Plain may result in a lower LUE. That may explain the more notable difference in slopes of NIRvP-GPP relationship for grass and crop we found than other studies. It needs to be noted that, for site level analysis, the difference in the footprints of spectral and flux observation can strongly affect the relationship of NIRvP and SIF (eSIF) with GPP (Kong et al., 2022). The difference in slopes in Fig. 10 (c) is larger than that in Fig. 10 (b) (satellite eSIF-GPP relationship) and Fig. 11(c) (in situ SIF-GPP relationship), which may be partly caused by the relatively large noise in original satellite SIF (the $R^2$ is only 0.11). For the data used in Fig. 11, both XTS site and AR site have homogeneous landcover, and the instruments have been cross-calibrated. So it is reasonable to assume the data at the two sites are comparable.

Among forest PFTs, eSIF did not show more universal relationship with GPP than NIRvP, which may due to the important role of canopy structure for forest PFTs. The relatively large variation of slopes among forest PFTs may partly explain the non-linear relationship of NIRvP-GPP and eSIF-GPP. Especially, the slopes of NIRvP-GPP and eSIF-GPP relationships for BoENF are much larger than that for other PFTs (Fig. 9). As shown in Fig. S7, the larger slopes for BoENF are caused by the relatively lower NIRvP and eSIF. The near-infrared canopy reflectance for needleleaf forest is usually lower than that for broadleaf forest (Ollinger, 2011; Knyazikhin et al., 2013), and hence, leads to a lower $f_{esc}$

for needleleaf forest. Moreover, BoENF mainly located at high-latitude regions, where PAR is relatively low. But APAR is usually excessive for photosynthesis, and SIF has been found to have more linear relationship with APAR than GPP (i.e., GPP would saturate with increase of APAR but SIF would not) (Zhang et al., 2016b; Kim et al., 2021). These facts may partly explain the much larger slopes of NIRvP-GPP and eSIF-GPP relationships for BoENF.

It needs to be noted that, as NIRvP contains the information of $f_{esc}$, eSIF still represent SIF at canopy level, instead of the total SIF emission, which means that the influence of canopy resorption and scattering effects is not removed. This problem might also be the reason for the varying eSIF–GPP regression slopes among different forest PFTs, and between forest and grass/crop PFTs. The different SIF–GPP relationships for woody and herbaceous vegetation were also reported by Pickering et al. (2022). We did not try to calculate the total SIF at the leaf or photosystem level because there are still large uncertainties in the estimation of $f_{esc}$ (Liu et al., 2019; Yang and van der Tol, 2018; Zeng et al., 2019) and $f$APAR (Zheng et al., 2018), especially on the global scale. Moreover, as introduced in Section 1, whether $f_{esc}$ has a positive or negative influence on the SIF–GPP relationship is still unclear.

The PFT-dependency for relationship of NIRvP and eSIF with GPP can partly explain the non-linearity of the relationships, especially for forest PFTs, as shown in Fig. 6. Moreover, the different response of $\Phi_F$ and LUE to APAR is another important reason for the non-linear relationships. LUE has been found to decrease with increasing APAR due to the photosynthesis saturation and the so-called “diffuse radiation fertilization” effect (Gu et al., 2002). For forest ecosystems, the understory vegetation contributes more to GPP than to APAR (and reflected radiation), because the diffuse radiation reached understory is sufficient for their photosynthesis. Differently, $\Phi_F$ has been found more stable than LUE with varying APAR (Gu et al., 2019; Kim et al., 2021; Liu et al., 2021), and SIF emitted by understory vegetation is difficult to be observed at top of canopy. The non-linearity of the relationships of NIRvP and eSIF with GPP is an important limitation for the GPP estimation models. To better understand the non-linearity of the relationships of NIRvP and eSIF with GPP, further investigation on the influence by structural and physiological factors is needed.

### 4.3. Difference between eSIF and existing reconstructed SIF products

As introduced in Section 1, several reconstructed SIF products (including CSIF (Zhang et al., 2018a), RSIF (Gentine and Alemohammad, 2018), GOSIF (Li and Xiao, 2019), downscaled SIF (Duveiller and Cescatti, 2016; Duveiller et al., 2020; Ma et al., 2022), SIFnet (Gensheimer et al., 2022), etc) have been developed to overcome the limitations caused by the low data quality of original satellite-based SIF products. These products have similar spatial and temporal resolutions with eSIF, and good correlations of them with GPP have been reported. Therefore, taken GOSIF product as an example, we compared the performance of eSIF and the reconstructed SIF for estimating GPP, as shown in Fig. S8-S11.

From Fig. S8 and Fig. S9, we can see that GOSIF shows better spatio-temporal correlations with FLUXCOM GPP than eSIF for both forest and grass/crop PFTs, and better temporal correlations for most areas. And by comparing Fig. S10 and Fig. 8, we can see that GOSIF shows better correlation with AmeriFlux GPP than eSIF for all single sites, but when pooling data at all sites, eSIF outperforms GOSIF. In Fig. S11, GOSIF shows similar seasonal pattern with eSIF for BoENF, but much smaller seasonal variation than eSIF for TrC3GRA, which indicates that eSIF performs better than GOSIF for tracking the seasonal variation of GPP for TrC3GRA.

The existing reconstructed SIF products are mainly based on MODIS reflectance, meteorological parameters, and vegetation types, which can represent the major driving factors of both SIF and GPP, and have much better data quality than original satellite-based SIF products. That may be the reason why the reconstructed SIF products showed good correlation with GPP. However, these reconstructed SIF products were generated using machine learning methods to model the relationship of SIF and the predictor variables. Therefore, strictly speaking, these reconstructed SIF products are only “simulated” SIF, but not “real” SIF. To better maintain the information in original SIF signal, Duveiller et al. (2020) calibrated the SIF predicting model in local spatio-temporal window, but it was still a data-driven method which could not give a clear relationship between the original and reconstructed SIF.

Different with the existing reconstructed SIF products which use a “black box” to describe the relationship between them and the original SIF, eSIF has much simpler and clearer relationship with original SIF, as the information of $\Phi_F$ is directly from the original SIF product. This characteristic (closer to “real” SIF) makes eSIF more appropriate to be used for the quantitative analysis on the relationship between SIF and GPP. For example, as shown in Fig. S11, although GOSIF have used VPD as one of its predicting variables, it still shows worse performance than eSIF for tracking the decrease of GPP for TrC3GRA in dry season. But at the same time, more errors and noise in original SIF are also transferred to eSIF, and results in a worse data quality, and consequently, generally worse relationship with GPP, than other reconstructed SIF products.

The major aim of the existing reconstructed SIF products is to improve the spatio-temporal resolution of original satellite-based SIF products. For example, to generate continuous global SIF product from the sparse observations of OCO-2, or to improve the spatial resolution of GOME-2 SIF product from 0.5° to 0.05°. Differently, eSIF does not aim to improve the spatio-temporal resolution of original SIF, but mainly aim to improve its data quality by reducing the noise, normalizing the directional effect, and transferring instantaneous SIF observation to multi-day average based on PAR.

To sum up, although eSIF does not show significant advantages over the existing reconstructed SIF products, it has much simpler and clearer relationship with original SIF, and is more appropriate to be used for the study on linkage between “real” SIF and GPP. Moreover, this study would also contribute to clarify the complementarity of SIF and NIRvP.

### 4.4. Uncertainties in the smoothing of $\Phi_F'$

As shown in Fig. S12, the estimated $\Phi_F'$ with 0.05°/8-day resolution still suffers from relatively large noise and invalid values. To generate a spatially continuous and less noisy eSIF product, a gaussian-weighted moving average filter was used in the spatial dimension to smooth $\Phi_F'$, which would have some influence on the spatial precision of $\Phi_F'$, especially for heterogeneous regions.

It is apparent that larger smoothing window would result in less noise but more loss of information. To determine the optimal size of smoothing window, we analyzed the distribution of the smoothed $\Phi_F'$ using different sizes of windows across PFTs and Longitudes (Fig. S13-S14). Fig. S13 shows the Boxplots of $\Phi_F'$ on 28 July 2019 for different PFTs in the Northern Hemisphere with different sizes (non-smoothing, 3 × 3, 5 × 5, and 7 × 7 pixels) of smoothing windows. As the selected sample pixels for each PFT are with a relatively homogeneous coverage, the variation of $\Phi_F'$ within specific PFT is expected to be small, and hence, it is reasonable to regard the outliers in the boxplots as noise. It can be seen from Fig. S13 that, the variation of 5 × 5 smoothed $\Phi_F'$ within specific PFT is notably smaller (the mean standard deviation is 0.0055) than that of 3 × 3 smoothed (the mean standard deviation is 0.0077) and non-smoothed $\Phi_F'$ (the mean standard deviation is 0.0061), while the difference between 5 × 5 and 7 × 7 smoothed $\Phi_F'$ is relatively small, which indicates that the 5 × 5 smoothing window is suitable for reducing the noise. On the other hand, the medians of $\Phi_F'$ for different PFTs do not change apparently with the increase of smoothing window size, which indicates small loss of key information. Fig. S14 shows the radial distribution profiles of $\Phi_F'$ on 28 July 2019 with different sizes of smoothing windows and non-smoothed NDVI at 40°N across the Eurasian Continent. NDVI is with relatively high signal-to-noise ratio and is consequently used as a reference to indicate the noise level in the

$\Phi_F'$ profiles. The profiles of non-smoothed and 3 × 3 smoothed $\Phi_F'$ are apparently noisier than that of NDVI, while for the 5 × 5 smoothed $\Phi_F'$, the noise is efficiently reduced. Meanwhile, taking the radial variation features in the NDVI profile as a reference, we can see that most of the valid features have been well kept in the profile of the 5 × 5 smoothed $\Phi_F'$. These results indicate that the 5 × 5 pixels smoothing window is suitable to reduce the noise in $\Phi_F'$ without critical loss of valid information.

Moreover, as reported by Dechant et al. (2022), the spatial variation in $\Phi_F$ was expected to be smaller than NIRvP. Therefore, compared to directly smoothing raw SIF (which means smoothing both $\Phi_F'$ and NIRvP), only smoothing $\Phi_F'$ would results in less loss of information, as shown in Fig. S2. But it needs to be noted that, in this study, as the relative performance of eSIF, SIF, and NIRvP for estimating GPP was tested using selected sample pixels with a relatively homogeneous coverage of dominate PFTs, the performance of the framework for generating eSIF over heterogeneous regions was not fully tested.

Alternatively, the smoothing of $\Phi_F'$ can be done in temporal dimension. We also tested using a gaussian-weighted moving average filter with time window of 5 epochs (composed $\Phi_F'$ with 8-day resolution for each epoch) to smooth the $\Phi_F'$, and consequently, generated another enhanced SIF product named as $\text{eSIF}_\text{T}$. Fig. S15 shows the spatio-temporal correlations of $\text{eSIF}_\text{T}$ with FLUXCOM GPP, and Fig. S16 shows the seasonal variations of $\text{eSIF}_\text{T}$ compared with eSIF for BoENF and TrC3GRA. These results indicate that $\text{eSIF}_\text{T}$ (temporally smoothed) is almost the same as eSIF (spatially smoothed) in the performance for tracking GPP. In Fig. S16, we can see that the seasonal variation of $\text{eSIF}_\text{T}$ is, unsurprisingly, smoother than that of eSIF. But we do not have enough evidence to determine whether any important temporal information in $\Phi_F'$ is lost due to the smoothing.

To conclude, both spatial and temporal smoothing have advantages and disadvantages, and further understanding of the spatial and temporal sensitivity of $\Phi_F$ is needed to determine which method is better for practice (or for specific aims). The results based on the spatially smoothed $\Phi_F'$ also indicated the potential of the methodology to be applied to improving the spatial resolution of SIF products (i.e., by integrating SIF products with low spatial resolution with NIRvP with high spatial resolution).

### 4.5. Limitations and perspectives

As introduced in Section 2.3.1, in the generation of eSIF based on the TROPOSIF product, multi-source datasets were used. In the calculation of $\Phi_F'$, the near-infrared $\text{TOA}_\text{Rad}$ (the product of TOA reflectance and near-infrared irradiance ($\text{Irr}_\text{NIR}$)) from the TROPOSIF product was used to represent the bi-directional characteristics of SIF; meanwhile, for the reconstruction of eSIF, PAR estimated using shortwave radiation from the ERA5 dataset and surface near-infrared reflectance from the MCD43C4 product was used. Although PAR and $\text{Irr}_\text{NIR}$ are closely correlated (Dechant et al., 2020; Zeng et al., 2022a) and their units were unified in this study, the difference between PAR and $\text{Irr}_\text{NIR}$ affect the value of the calculated eSIF. Nevertheless, ignoring the slight influence of varying the ratio of diffuse radiation on the PAR–$\text{Irr}_\text{NIR}$ relationship (only observations with cloud fraction lower than 0.2 were used in this study), the ratio of PAR to $\text{Irr}_\text{NIR}$ (over 743–758 nm) would be close to constant and would have little influence on the relationship between eSIF and GPP.

The MODIS NBAR product was used for the calculation of eSIF to deal with the directional effect, but MODIS NBAR product did not normalize the effect of solar zenith angle (SZA). Moreover, as TROPOSIF product only provided TOA reflectance, NDVI from MODIS NBAR product was used instead for the calculation of $\Phi_F'$ from TROPOSIF, which meant that the directional effect on NDVI was ignored. Using multi-angular simulations by SCOPE model for a canopy with spherical leaf inclination distribution, LAI of 2 and chlorophyll $a$ + b content of 40 $\mu\text{g/cm}^2$, we found that the CV of NIR reflectance is only 1.17% when solar zenith angle (SZA) varies from 10° to 60° for nadir observation. When changing view zenith angle (VZA) from 10° to 60° (SZA = 30°, relative azimuth angle = 90°), the CV of NIR reflectance is 4.81%, and the CV of NDVI is 2.77%. These results indicated that the VZA-dependent NIR reflectance is the major problem needs to be dealt with. Zeng et al. (2022b) also claimed that NDVI was less impacted by the imaging geometry than NIRv, which meant the directional characteristics of NIRv was mainly caused by the NIR reflectance. Therefore, to keep the algorithm simple and avoid introducing more uncertainties, we selected the widely used MODIS NBAR product and did not do additional directional normalization, which is similar as the strategy used in relevant studies (e.g., Dechant et al., 2022). It also needs to be noted that, the bi-directional characteristics of NIR SIF and reflectance are similar but not identical (Hao et al., 2021), which means that the directional effect in $\Phi_F'$ is not fully removed. But the reflectance-based method for directional normalization of SIF has been widely used and proven to be efficient (e.g., Zeng et al., 2019; Hao et al., 2021; Hao et al., 2022).

$\Phi_F'$ was calculated using the ratio of SIF to NIRvP (Zeng et al., 2022a). For pixels with low vegetation coverage, both the values of SIF and NIRvP would be close to zero, which would lead to large uncertainties in $\Phi_F'$. With a large enough number of samples, using the linear regression slopes of SIF to NIRvP instead of their ratio might be efficient to reduce the uncertainties in $\Phi_F'$ (Dechant et al., 2022; Zeng et al., 2022a), but as this study was conducted in a 0.05°/8-day resolutions, the number of samples (<8 for most grid cells) was not enough for a reliable linear regression. Alternatively, we used the median of $\Phi_F'$ in each grid to reduce the uncertainties. With NIRvP close to zero, the uncertainties in $\Phi_F'$ for low vegetation-covered pixels would have little influence on eSIF, especially after filtering and smoothing of outliers.

The results of this study mainly relied on the FLUXCOM GPP product, which was a machine learning based upscaled product, and would suffer from its own uncertainties. Although GPP data at site level were also tested, the amount and representativeness of the dataset was quite limited, and the difference in the footprints of NIRvP, eSIF, SIF and GPP may lead to uncertainties to the results. Therefore, in future work, more site and global scales (e.g., FLUXSAT GPP (Joiner et al., 2018), GLASS GPP (Yuan et al., 2010; Liang et al., 2021)) datasets, and more accurate scale match between GPP and NIRvP, eSIF, or SIF data should be conducted. Additionally, as we mainly aimed to compare the optical (or structural) and physiological components of SIF (NIRvP vs. $\Phi_F$), the performance of eSIF and SIF for GPP estimation was only compared with NIRvP. However, as reported by Joiner and Yoshida (2020), other reflectance-based vegetation indices generated by neural network method outperformed NIRv for GPP estimation. So a more comprehensive evaluation of the potential for eSIF needs to be conducted by comparing with other indicators of GPP.

With the development of satellite-based sensors, more and more SIF observations with higher data quality can be achieved. For example, OCO-3 onboard the International Space Station (ISS) can provide multi-observations for the same point in one day (Taylor et al., 2020), which provide opportunities to better explore the diurnal variation of SIF and $\Phi_F$; the Fluorescence Explorer (FLEX) mission (expected to be launched in 2025) is designed to provide global SIF observations with spatial resolution of 300 m, which would be helpful to better investigate the spatial patterns of SIF and $\Phi_F$. However, it is difficult to get SIF observation with high spatial and temporal resolution from single sensor, and the calibration errors and different overpass time would make it difficult to use multi-source SIF data directly. In addition, the sensor degradation is an important uncertainty for long-term SIF observations (such as GOME-2 SIF) (Parazoo et al., 2019). Compared to SIF, $\Phi_F$ is much less influenced by these factors, and the methodology of this study has potential for integrating multi-source SIF, reflectance, and radiation products.

## 5. Conclusion

SIF and NIRvP have complementary advantages for GPP estimation. Compared to NIRvP, SIF has unique physiological information that can better track the variation in LUE due to environmental stress, but the data quality and availability of SIF are much lower than that of NIRvP. We have proposed a framework to generate an enhanced SIF product (eSIF) with a spatial resolution of 0.05° and a temporal resolution of 8 days using multi-source datasets by combining the information of the optical (NIRvP) and physiological ($\Phi_F$) components of SIF. With this framework, the drawbacks of SIF related to high retrieval noise, directional dependency, and time-scale mismatch with independant GPP estimates could be efficiently reduced. eSIF showed similar spatial patterns as the original SIF data, but has smoother spatial variation and is less noisy. Compared to NIRvP, eSIF was shown to better track the variation in GPP due to environmental stresses as well as to have more potential as a universal proxy of GPP among different grass/crop PFTs, while NIRvP showed more potential for tracking GPP for forest PFTs (exclude BoENF). In summary, combining SIF with NIRvP is a promising way for better monitoring GPP.

## CRediT authorship contribution statement

**Xinjie Liu:** Conceptualization, Methodology, Formal analysis, Writing – original draft, Funding acquisition. **Liangyun Liu:** Conceptualization, Writing – review & editing, Supervision, Funding acquisition. **Cédric Bacour:** Resources, Writing – review & editing. **Luis Guanter:** Resources, Writing – review & editing. **Jidai Chen:** Software, Resources. **Yan Ma:** Resources, Investigation. **Ruonan Chen:** Resources, Investigation. **Shanshan Du:** Validation, Writing – review & editing.

## Declaration of Competing Interest

The authors declare that they have no known competing financial interests or personal relationships that could have appeared to influence the work reported in this paper.

## Data availability

eSIF products are available at https://doi.org/10.5281/zenodo.6115416. TROPOSIF products are available at http://ftp.sron.nl/open-access-data-2/TROPOMI/tropomi/sif/v2.1/l2b/. MCD43C4 products are available at https://earthdata.nasa.gov/. ERA5 datasets are available at https://cds.climate.copernicus.eu/. FLUXCOM GPP products are available from Dr. Martin Jung (mjung@bgc-jena.mpg.de). GOSIF products are available at http://globalecology.unh.edu/. AmeriFlux sites data is available at https://ameriflux.lbl.gov/. The in situ SIF and GPP datasets at XTS and DM sites are available from the authors upon request.

## Acknowledgments

This research was funded by the Innovative Research Program of the International Research Center of Big Data for Sustainable Development Goals (CBAS2022ORP03), and the National Natural Science Foundation of China (42071310, 41825002). We thank Dr. Martin Jung and Ulrich Weber for providing the FLUXCOM GPP products, and we thank Prof. Guijun Yang, Prof. Shaomin Liu, and Dr. Ziwei Xu for providing the in situ GPP datasets.

## Appendix A. Supplementary data

Supplementary data to this article can be found online at https://doi.org/10.1016/j.rse.2022.113341.

## References

Asner, G.P., Wessman, C.A., 1997. Scaling PAR absorption from the leaf to landscape level in spatially heterogeneous ecosystems. Ecol. Model. 103 (1), 81–97.

Asner, G.P., 1998. Biophysical and biochemical sources of variability in canopy reflectance. Remote Sens. Environ. 64 (3), 234–253.

Bacour, C., Maignan, F., Peylin, P., MacBean, N., Bastrikov, V., Joiner, J., Köhler, P., Guanter, L., Frankenberg, C., 2019. Differences between OCO-2 and GOME-2 SIF products from a model-data fusion perspective. J.Geophys.Res.Biogeosci. 124, 3143–3157.

Badgley, G., Field, C.B., Berry, J.A., 2017. Canopy near-infrared reflectance and terrestrial photosynthesis. Sci. Adv. 3, e1602244.

Badgley, G., Anderegg, L.D.L., Berry, J.A., Field, C.B., 2019. Terrestrial gross primary production: using NIRV to scale from site to globe. Glob. Chang. Biol. 25, 3731–3740.

Baldocchi, D.D., Ryu, Y., Dechant, B., Eichelmann, E., Hemes, K., Ma, S., Sanchez, C.R., Shortt, R., Szutu, D., Valach, A., Verfaillie, J., Badgley, G., Zeng, Y., Berry, J.A., 2020. Outgoing near-infrared radiation from vegetation scales with canopy photosynthesis across a spectrum of function, structure, physiological capacity, and weather. J. Geophys. Res. Biogeosci. 125.

Buck, A.L., 1981. New equations for computing vapor pressure and enhancement factor. J. Appl. Meteorol. Climatol. 20, 1527–1532.

Cui, Y., Xiao, X., Dong, J., Zhang, Y., Qin, Y., Doughty, R.B., Wu, X., Liu, X., Joiner, J., Moore, B., 2022. Continued increases of gross primary production in urban areas during 2000 - 2016. J. Remote Sens. 2022.

Damm, A., Erler, A., Hillen, W., Meroni, M., Schaepman, M.E., Verhoef, W., Rascher, U., 2011. Modeling the impact of spectral sensor configurations on the FLD retrieval accuracy of sun-induced chlorophyll fluorescence. Remote Sens. Environ. 115, 1882–1892.

Damm, A., Guanter, L., Verhoef, W., Schläpfer, D., Garbari, S., Schaepman, M.E., 2015. Impact of varying irradiance on vegetation indices and chlorophyll fluorescence derived from spectroscopy data. Remote Sens. Environ. 156, 202–215.

Dechant, B., Ryu, Y., Badgley, G., Köhler, P., Rascher, U., Migliavacca, M., Zhang, Y., Tagliabue, G., Guan, K., Rossini, M., Goulas, Y., Zeng, Y., Frankenberg, C., Berry, J. A., 2022. NIRVP: a robust structural proxy for sun-induced chlorophyll fluorescence and photosynthesis across scales. Remote Sens. Environ. 268, 112763.

Dechant, B., Ryu, Y., Badgley, G., Zeng, Y., Berry, J.A., Zhang, Y., Goulas, Y., Li, Z., Zhang, Q., Kang, M., 2020. Canopy structure explains the relationship between photosynthesis and sun-induced chlorophyll fluorescence in crops. Remote Sens. Environ. 241, 111733.

Du, S., Liu, L., Liu, X., Zhang, X., Zhang, X., Bi, Y., Zhang, L., 2018. Retrieval of global terrestrial solar-induced chlorophyll fluorescence from TanSat satellite. Sci.Bull. 63, 1502–1512.

Du, S., Liu, L., Liu, X., Guo, J., Hu, J., Wang, S., Zhang, Y., 2019. SIFSpec: measuring solar-induced chlorophyll fluorescence observations for remote sensing of photosynthesis. Sensors 19, 3009.

Duveiller, G., Cescatti, A., 2016. Spatially downscaling sun-induced chlorophyll fluorescence leads to an improved temporal correlation with gross primary productivity. Remote Sens. Environ. 182, 72–89.

Duveiller, G., Filipponi, F., Walther, S., Köhler, P., Frankenberg, C., Guanter, L., Cescatti, A., 2020. A spatially downscaled sun-induced fluorescence global product for enhanced monitoring of vegetation productivity. Earth Syst.Sci.Data 12, 1101–1116.

Falge, E., Baldocchi, D., Olson, R., Anthoni, P., Aubinet, M., Bernhofer, C., Burba, G., Ceulemans, R., Clement, R., Dolman, H., 2001. Gap filling strategies for defensible annual sums of net ecosystem exchange. Agric. For. Meteorol. 107, 43–69.

Frankenberg, C., Berry, J., 2018. Solar induced chlorophyll fluorescence: origins, relation to photosynthesis and retrieval. In: Reference Module in Earth Systems and Environmental Sciences. Elsevier, pp. 143–162.

Frankenberg, C., Fisher, J.B., Worden, J., Badgley, G., Saatchi, S.S., Lee, J.-E., Toon, G.C., Butz, A., Jung, M., Kuze, A., Yokota, T., 2011. New global observations of the terrestrial carbon cycle from GOSAT: patterns of plant fluorescence with gross primary productivity. Geophys. Res. Lett. 38.

Frankenberg, C., O'Dell, C., Berry, J., Guanter, L., Joiner, J., Köhler, P., Pollock, R., Taylor, T.E., 2014. Prospects for chlorophyll fluorescence remote sensing from the Orbiting Carbon Observatory-2. Remote Sens. Environ. 147, 1–12.

Gensheimer, J., Turner, A.J., Köhler, P., Frankenberg, C., Chen, J., 2022. A convolutional neural network for spatial downscaling of satellite-based solar-induced chlorophyll fluorescence (SIFnet). Biogeosciences 19, 1777–1793.

Gentine, P., Alemohammad, S.H., 2018. Reconstructed solar-induced fluorescence: a machine learning vegetation product based on MODIS surface reflectance to reproduce GOME-2 solar-induced fluorescence. Geophys. Res. Lett. 45, 3136–3146.

Gu, L., Baldocchi, D., Verma, S.B., Black, T.A., Vesala, T., Falge, E.M., Dowty, P.R., 2002. Advantages of diffuse radiation for terrestrial ecosystem productivity. J. Geophys. Res. Atmos. 107, ACL 2-1–ACL 2-23.

Gu, L., Han, J., Wood, J.D., Chang, C.Y., Sun, Y., 2019. Sun-induced Chl fluorescence and its importance for biophysical modeling of photosynthesis based on light reactions. New Phytol. 223, 1179–1191.

Guanter, L., Aben, I., Tol, P., Krijger, J.M., Hollstein, A., Köhler, P., Damm, A., Joiner, J., Frankenberg, C., Landgraf, J., 2015. Potential of the TROPOspheric Monitoring Instrument (TROPOMI) onboard the Sentinel-5 precursor for the monitoring of terrestrial chlorophyll fluorescence. Atmos.Meas.Tech. 8, 1337–1352.

Guanter, L., Bacour, C., Schneider, A., Aben, I., van Kempen, T.A., Maignan, F., Retscher, C., Köhler, P., Frankenberg, C., Joiner, J., 2021. The TROPOSIF global sun-induced fluorescence dataset from the Sentinel-5P TROPOMI mission. Earth Syst.Sci. Data 13, 5423–5440.

Guanter, L., Zhang, Y., Jung, M., Joiner, J., Voigt, M., Berry, J.A., Frankenberg, C., Huete, A.R., Zarco-Tejada, P., Lee, J.-E., 2014. Global and time-resolved monitoring of crop photosynthesis with chlorophyll fluorescence. Proc. Natl. Acad. Sci. 201320008.

Hao, D., Zeng, Y., Qiu, H., Biriukova, K., Celesti, M., Migliavacca, M., Chen, M., 2021. Practical approaches for normalizing directional solar-induced fluorescence to a standard viewing geometry. Remote Sens. Environ. 255, 112171.

Hao, D., Zeng, Y., Zhang, Z., Zhang, Y., Qiu, H., Biriukova, K., Chen, M., 2022. Adjusting solar-induced fluorescence to nadir-viewing provides a better proxy for GPP. ISPRS J. Photogramm. Remote Sens. 186, 157–169.

Hu, J., Liu, L., Yu, H., Guan, L., Liu, X., 2021. Upscaling GOME-2 SIF from clear-sky instantaneous observations to all-sky sums leading to an improved SIF–GPP correlation. Agric. For. Meteorol. 306, 108439.

Jacovides, C., Tymvios, F., Asimakopoulos, D., Theofilou, K., Pashiardes, S., 2003. Global photosynthetically active radiation and its relationship with global solar radiation in the Eastern Mediterranean basin. Theor. Appl. Climatol. 74, 227–233.

Jiang, C., Guan, K., Wu, G., Peng, B., Wang, S., 2021. A daily, 250 m and real-time gross primary productivity product (2000–present) covering the contiguous United States. Earth Syst.Sci.Data 13, 281–298.

Joiner, J., Yoshida, Y., Vasilkov, A.P., Corp, L.A., Middleton, E.M., 2011. First observations of global and seasonal terrestrial chlorophyll fluorescence from space. Biogeosciences 8, 637–651.

Joiner, J., Yoshida, Y., Vasilkov, A.P., Schaefer, K., Jung, M., Guanter, L., Zhang, Y., Garrity, S., Middleton, E.M., Huemmrich, K.F., Gu, L., Belelli Marchesini, L., 2014. The seasonal cycle of satellite chlorophyll fluorescence observations and its relationship to vegetation phenology and ecosystem atmosphere carbon exchange. Remote Sens. Environ. 152, 375–391.

Joiner, J., Yoshida, Y., Guanter, L., Middleton, E.M., 2016. New methods for the retrieval of chlorophyll red fluorescence from hyperspectral satellite instruments: simulations and application to GOME-2 and SCIAMACHY. Atmos.Meas.Tech. 9, 3939–3967.

Joiner, J., Yoshida, Y., 2020. Satellite-based reflectances capture large fraction of variability in global gross primary production (GPP) at weekly time scales. Agric. For. Meteorol. 291, 108092.

Joiner, J., Yoshida, Y., Zhang, Y., Duveiller, G., Jung, M., Lyapustin, A., Wang, Y., Tucker, C., 2018. Estimation of terrestrial global gross primary production (GPP) with satellite data-driven models and Eddy covariance flux data. Remote Sens. 10, 1346.

Jonard, F., De Cannière, S., Brüggemann, N., Gentine, P., Short Gianotti, D.J., Lobet, G., Miralles, D.G., Montzka, C., Pagán, B.R., Rascher, U., Vereecken, H., 2020. Value of sun-induced chlorophyll fluorescence for quantifying hydrological states and fluxes: current status and challenges. Agric. For. Meteorol. 291, 108088.

Jung, M., Koirala, S., Weber, U., Ichii, K., Gans, F., Camps-Valls, G., Papale, D., Schwalm, C., Tramontana, G., Reichstein, M., 2019. The FLUXCOM ensemble of global land-atmosphere energy fluxes. Sci. Data 6, 74.

Jung, M., Schwalm, C., Migliavacca, M., Walther, S., Camps-Valls, G., Koirala, S., Anthoni, P., Besnard, S., Bodesheim, P., Carvalhais, N., Chevallier, F., Gans, F., Goll, D.S., Haverd, V., Köhler, P., Ichii, K., Jain, A.K., Liu, J., Lombardozzi, D., Nabel, J.E.M.S., Nelson, J.A., O'Sullivan, M., Pallandt, M., Papale, D., Peters, W., Pongratz, J., Rödenbeck, C., Sitch, S., Tramontana, G., Walker, A., Weber, U., Reichstein, M., 2020. Scaling carbon fluxes from eddy covariance sites to globe: synthesis and evaluation of the FLUXCOM approach. Biogeosciences 17, 1343–1365.

Khan, A.M., Stoy, P.C., Joiner, J., Baldocchi, D., Verfaillie, J., Chen, M., Otkin, J.A., 2022. The diurnal dynamics of gross primary productivity using observations from the advanced baseline imager on the geostationary operational environmental satellite-R series at an oak savanna ecosystem. J. Geophys. Res. Biogeosci. 127 (3), e2021JG006701.

Knyazikhin, Y., Schull, M.A., Stenberg, P., Mõttus, M., Rautiainen, M., Yang, Y., Marshak, A., Carmona, P.L., Kaufmann, R.K., Lewis, P., 2013. Hyperspectral remote sensing of foliar nitrogen content. Proc. Natl. Acad. Sci. 110, E185–E192.

Kong, J., Ryu, Y., Liu, J., Dechant, B., Rey-Sanchez, C., Shortt, R., Szutu, D., Verfaillie, J., Houborg, R., Baldocchi, D.D., 2022. Matching high resolution satellite data and flux tower footprints improves their agreement in photosynthesis estimates. Agric. For. Meteorol. 316, 108878.

Köhler, P., Frankenberg, C., Magney, T.S., Guanter, L., Joiner, J., Landgraf, J., 2018. Global retrievals of solar-induced chlorophyll fluorescence with TROPOMI: first results and intersensor comparison to OCO-2. Geophys. Res. Lett. 45, 10,456–410,463.

Köhler, P., Guanter, L., Joiner, J., 2015. A linear method for the retrieval of sun-induced chlorophyll fluorescence from GOME-2 and SCIAMACHY data. Atmos.Meas.Tech. 8, 2589–2608.

Kim, J., Ryu, Y., Dechant, B., Lee, H., Kim, H.S., Kornfeld, A., Berry, J.A., 2021. Solar-induced chlorophyll fluorescence is non-linearly related to canopy photosynthesis in a temperate evergreen needleleaf forest during the fall transition. Remote Sens. Environ. 258, 112362.

Kimm, H., Guan, K., Jiang, C., Miao, G., Wu, G., Suyker, A.E., Ainsworth, E.A., Bernacchi, C.J., Montes, C.M., Berry, J.A., Yang, X., Frankenberg, C., Chen, M., Köhler, P., 2021. A physiological signal derived from sun-induced chlorophyll fluorescence quantifies crop physiological response to environmental stresses in the U.S. Corn Belt. Environ. Res. Lett. 16, 124051.

Li, X., Xiao, J., 2019. A global, 0.05-degree product of solar-induced chlorophyll fluorescence derived from OCO-2, MODIS, and reanalysis data. Remote Sens. 11, 517.

Li, X., Xiao, J., 2022. TROPOMI observations allow for robust exploration of the relationship between solar-induced chlorophyll fluorescence and terrestrial gross primary production. Remote Sens. Environ. 268, 112748.

Liang, S., Cheng, J., Jia, K., Jiang, B., Liu, Q., Xiao, Z., Yao, Y., Yuan, W., Zhang, X., Zhao, X., 2021. The global land surface satellite (GLASS) product suite. Bull. Am. Meteorol. Soc. 102, E323–E337.

Liu, L., Liu, X., Chen, J., Du, S., Ma, Y., Qian, X., Chen, S., Peng, D., 2020. Estimating maize GPP using near-infrared radiance of vegetation. Sci.Remote Sens. 2, 100009.

Liu, L., Liu, X., Hu, J., 2015. Effects of spectral resolution and SNR on the vegetation solar-induced fluorescence retrieval using FLD-based methods at canopy level. Eur.J. Remote Sens. 48, 743–762.

Liu, S., Li, X., Xu, Z., Che, T., Xiao, Q., Ma, M., Liu, Q., Jin, R., Guo, J., Wang, L., 2018. The Heihe Integrated Observatory Network: a basin-scale land surface processes observatory in China. Vadose Zone J. 17.

Liu, S., Xu, Z., Wang, W., Jia, Z., Zhu, M., Bai, J., Wang, J., 2011. A comparison of eddy-covariance and large aperture scintillometer measurements with respect to the energy balance closure problem. Hydrol. Earth Syst. Sci. 15, 1291–1306.

Liu, X., Guanter, L., Liu, L., Damm, A., Malenovský, Z., Rascher, U., Peng, D., Du, S., Gastellu-Etchegorry, J.-P., 2019. Downscaling of solar-induced chlorophyll fluorescence from canopy level to photosystem level using a random forest model. Remote Sens. Environ. 231, 110772.

Liu, X., Liu, L., 2014. Assessing band sensitivity to atmospheric radiation transfer for space-based retrieval of solar-induced chlorophyll fluorescence. Remote Sens. 6, 10656–10675.

Liu, X., Liu, Z., Liu, L., Lu, X., Chen, J., Du, S., Zou, C., 2021. Modelling the influence of incident radiation on the SIF-based GPP estimation for maize. Agric. For. Meteorol. 307, 108522.

Luo, X., Croft, H., Chen, J.M., He, L., Keenan, T.F., 2019. Improved estimates of global terrestrial photosynthesis using information on leaf chlorophyll content. Glob. Chang. Biol. 25 (7), 2499–2514.

Ma, Y., Liu, L., Liu, X., Chen, J., 2022. An improved downscaled sun-induced chlorophyll fluorescence (DSIF) product of GOME-2 dataset. Eur.J.Remote Sens. 55, 168–180.

Magney, T.S., Bowling, D.R., Logan, B.A., Grossmann, K., Stutz, J., Blanken, P.D., Burns, S.P., Cheng, R., Garcia, M.A., Khler, P., Lopez, S., Parazoo, N.C., Raczka, B., Schimel, D., Frankenberg, C., 2019. Mechanistic evidence for tracking the seasonality of photosynthesis with solar-induced fluorescence. Proc. Natl. Acad. Sci. U. S. A. 116, 11640–11645.

Maier, S.W., Günther, K.P., Stellmes, M., 2003. Sun-induced fluorescence: a new tool for precision farming. In: McDonald, M., Schepers, J., Tartly, L., Toai, T.v., Major, D. (Eds.), Digital Imaging and Spectral Techniques: Applications to Precision Agriculture and Crop Physiology. American Society of Agronomy Special Publication, Madison, WI, USA, pp. 209–222.

Martini, D., Sakowska, K., Wohlfahrt, G., Pacheco-Labrador, J., van der Tol, C., Porcar-Castell, A., Magney, T.S., Carrara, A., Colombo, R., El-Madany, T.S., Gonzalez-Cascon, R., Martin, M.P., Julitta, T., Moreno, G., Rascher, U., Reichstein, M., Rossini, M., Migliavacca, M., 2022. Heatwave breaks down the linearity between sun-induced fluorescence and gross primary production. New Phytol. 233, 2415–2428.

Meroni, M., Rossini, M., Guanter, L., Alonso, L., Rascher, U., Colombo, R., Moreno, J., 2009. Remote sensing of solar-induced chlorophyll fluorescence: review of methods and applications. Remote Sens. Environ. 113, 2037–2051.

Mohammed, G.H., Colombo, R., Middleton, E.M., Rascher, U., van der Tol, C., Nedbal, L., Goulas, Y., Pérez-Priego, O., Damm, A., Meroni, M., Joiner, J., Cogliati, S., Verhoef, W., Malenovský, Z., Gastellu-Etchegorry, J.-P., Miller, J.R., Guanter, L., Moreno, J., Moya, I., Berry, J.A., Frankenberg, C., Zarco-Tejada, P.J., 2019. Remote sensing of solar-induced chlorophyll fluorescence (SIF) in vegetation: 50 years of progress. Remote Sens. Environ. 231, 111177.

Muñoz-Sabater, J., Dutra, E., Agustí-Panareda, A., Albergel, C., Arduini, G., Balsamo, G., Boussetta, S., Choulga, M., Harrigan, S., Hersbach, H., 2021. ERA5-land: a state-of-the-art global reanalysis dataset for land applications. Earth Syst.Sci.Data Discuss. 1–50.

Ollinger, S.V., 2011. Sources of variability in canopy reflectance and the convergent properties of plants. New Phytol. 189, 375–394.

Parazoo, N.C., Frankenberg, C., Köhler, P., Joiner, J., Yoshida, Y., Magney, T., Sun, Y., Yadav, V., 2019. Towards a harmonized long-term spaceborne record of far-red solar-induced fluorescence. J. Geophys. Res. Biogeosci. 124, 2518–2539.

Peng, B., Guan, K., Zhou, W., Jiang, C., Frankenberg, C., Sun, Y., He, L., Köhler, P., 2020. Assessing the benefit of satellite-based solar-induced chlorophyll fluorescence in crop yield prediction. Int. J. Appl. Earth Obs. Geoinf. 90, 102126.

Pickering, M., Cescatti, A., Duveiller, G., 2022. Sun-induced fluorescence as a proxy of primary productivity across vegetation types and climates. Biogeosci. Discuss. 1–33.

Porcar-Castell, A., Malenovský, Z., Magney, T., Van Wittenberghe, S., Fernández-Marín, B., Maignan, F., Zhang, Y., Maseyk, K., Atherton, J., Albert, L.P., Robson, T. M., Zhao, F., Garcia-Plazaola, J.-I., Ensminger, I., Rajewicz, P.A., Grebe, S., Tikkanen, M., Kellner, J.R., Ihalainen, J.A., Rascher, U., Logan, B., 2021. Chlorophyll a fluorescence illuminates a path connecting plant molecular biology to Earth-system science. Nat. Plants 7, 998–1009.

Porcar-Castell, A., Tyystjärvi, E., Atherton, J., van der Tol, C., Flexas, J., Pfündel, E.E., Moreno, J., Frankenberg, C., Berry, J.A., 2014. Linking chlorophyll a fluorescence to photosynthesis for remote sensing applications: mechanisms and challenges. J. Exp. Bot. eru191.

Poulter, B., MacBean, N., Hartley, A., Khlystova, I., Arino, O., Betts, R., Bontemps, S., Boettcher, M., Brockmann, C., Defourny, P., Hagemann, S., Herold, M., Kirches, G., Lamarche, C., Lederer, D., Ottlé, C., Peters, M., Peylin, P., 2015. Plant functional type classification for earth system models: results from the European Space Agency's land cover climate change initiative. Geosci. Model Dev. 8, 2315–2328.

Reichstein, M., Falge, E., Baldocchi, D., Papale, D., Aubinet, M., Berbigier, P., Bernhofer, C., Buchmann, N., Gilmanov, T., Granier, A., 2005. On the separation of net ecosystem exchange into assimilation and ecosystem respiration: review and improved algorithm. Glob. Chang. Biol. 11, 1424–1439.

Ryu, Y., Berry, J.A., Baldocchi, D.D., 2019. What is global photosynthesis? History, uncertainties and opportunities. Remote Sens. Environ. 223, 95–114.

Ryu, Y., Jiang, C., Kobayashi, H., Detto, M., 2018. MODIS-derived global land products of shortwave radiation and diffuse and total photosynthetically active radiation at 5 km resolution from 2000. Remote Sens. Environ. 204, 812–825.

Schaaf, C., 2015. MCD43C4 MODIS/Terra+ Aqua BRDF-Adjusted Nadir Reflectance Daily L3 Global 0.05 Deg CMG V006. NASA EOSDIS Land Processes DAAC, Sioux Falls, SD, USA.

Sims, D.A., Rahman, A.F., Vermote, E.F., Jiang, Z., 2011. Seasonal and inter-annual variation in view angle effects on MODIS vegetation indices at three forest sites. Remote Sens. Environ. 115, 3112–3120.

Sun, Y., Frankenberg, C., Jung, M., Joiner, J., Guanter, L., Köhler, P., Magney, T., 2018. Overview of solar-induced chlorophyll fluorescence (SIF) from the orbiting carbon observatory-2: retrieval, cross-mission comparison, and global monitoring for GPP. Remote Sens. Environ. 209, 808–823.

Sun, Y., Frankenberg, C., Wood, J.D., Schimel, D., Jung, M., Guanter, L., Drewry, D., Verma, M., Porcar-Castell, A., Griffis, T.J., 2017. OCO-2 advances photosynthesis observation from space via solar-induced chlorophyll fluorescence. Science 358, eaam5747.

Taylor, T.E., Eldering, A., Merrelli, A., Kiel, M., Somkuti, P., Cheng, C., Rosenberg, R., Fisher, B., Crisp, D., Basilio, R., Bennett, M., Cervantes, D., Chang, A., Dang, L., Frankenberg, C., Haemmerle, V.R., Keller, G.R., Kurosu, T., Laughner, J.L., Lee, R., Marchetti, Y., Nelson, R.R., O'Dell, C.W., Osterman, G., Pavlick, R., Roehl, C., Schneider, R., Spiers, G., To, C., Wells, C., Wennberg, P.O., Yelamanchili, A., Yu, S., 2020. OCO-3 early mission operations and initial (vEarly) XCO2 and SIF retrievals. Remote Sens. Environ. 251, 112032.

Turner, A.J., Köhler, P., Magney, T.S., Frankenberg, C., Fung, I., Cohen, R.C., 2021. Extreme events driving year-to-year differences in gross primary productivity across the US. Biogeosciences 18, 6579–6588.

van der Tol, C., Vilfan, N., Dauwe, D., Cendrero-Mateo, M.P., Yang, P., 2019. The scattering and re-absorption of red and near-infrared chlorophyll fluorescence in the models fluspect and SCOPE. Remote Sens. Environ. 232, 111292.

Walther, S., Voigt, M., Thum, T., Gonsamo, A., Zhang, Y., Kohler, P., Jung, M., Varlagin, A., Guanter, L., 2016. Satellite chlorophyll fluorescence measurements reveal large-scale decoupling of photosynthesis and greenness dynamics in boreal evergreen forests. Glob. Chang. Biol. 22, 2979–2996.

Wieneke, S., Burkart, A., Cendrero-Mateo, M.P., Julitta, T., Rossini, M., Schickling, A., Schmidt, M., Rascher, U., 2018. Linking photosynthesis and sun-induced fluorescence at sub-daily to seasonal scales. Remote Sens. Environ. 219, 247–258.

Wohlfahrt, G., Gerdel, K., Migliavacca, M., Rotenberg, E., Tatarinov, F., Muller, J., Hammerle, A., Julitta, T., Spielmann, F.M., Yakir, D., 2018. Sun-induced fluorescence and gross primary productivity during a heat wave. Sci.Rep. 8, 14169.

Wu, G., Guan, K., Jiang, C., Peng, B., Kimm, H., Chen, M., Yang, X., Wang, S., Suyker, A. E., Bernacchi, C.J., Moore, C.E., Zeng, Y., Berry, J.A., Cendrero-Mateo, M.P., 2020. Radiance-based NIRv as a proxy for GPP of corn and soybean. Environ. Res. Lett. 15, 034009.

Xu, S., Atherton, J., Riikonen, A., Zhang, C., Oivukkamäki, J., MacArthur, A., Honkavaara, E., Hakala, T., Koivumäki, N., Liu, Z., 2021. Structural and photosynthetic dynamics mediate the response of SIF to water stress in a potato crop. Remote Sens. Environ. 263, 112555.

Yang, P., van der Tol, C., 2018. Linking canopy scattering of far-red sun-induced chlorophyll fluorescence with reflectance. Remote Sens. Environ. 209, 456–467.

Yang, P., van der Tol, C., Campbell, P.K.E., Middleton, E.M., 2021. Unraveling the physical and physiological basis for the solar- induced chlorophyll fluorescence and photosynthesis relationship using continuous leaf and canopy measurements of a corn crop. Biogeosciences 18, 441–465.

Yuan, W., Zheng, Y., Piao, S., Ciais, P., Lombardozzi, D., Wang, Y., Ryu, Y., Chen, G., Dong, W., Hu, Z., 2019. Increased atmospheric vapor pressure deficit reduces global vegetation growth. Sci. Adv. 5, eaax1396.

Yang, P., van der Tol, C., Verhoef, W., Damm, A., Schickling, A., Kraska, T., Muller, O., Rascher, U., 2019. Using reflectance to explain vegetation biochemical and structural effects on sun-induced chlorophyll fluorescence. Remote Sens. Environ. 231, 110996.

Yuan, W., Liu, S., Yu, G., Bonnefond, J.-M., Chen, J., Davis, K., Desai, A.R., Goldstein, A. H., Gianelle, D., Rossi, F., 2010. Global estimates of evapotranspiration and gross primary production based on MODIS and global meteorology data. Remote Sens. Environ. 114, 1416–1431.

Zeng, Y., Badgley, G., Dechant, B., Ryu, Y., Chen, M., Berry, J.A., 2019. A practical approach for estimating the escape ratio of near-infrared solar-induced chlorophyll fluorescence. Remote Sens. Environ. 111209.

Zeng, Y., Chen, M., Hao, D., Damm, A., Badgley, G., Rascher, U., Johnson, J.E., Dechant, B., Siegmann, B., Ryu, Y., Qiu, H., Krieger, V., Panigada, C., Celesti, M., Miglietta, F., Yang, X., Berry, J.A., 2022a. Combining near-infrared radiance of vegetation and fluorescence spectroscopy to detect effects of abiotic changes and stresses. Remote Sens. Environ. 270, 112856.

Zeng, Y., Hao, D., Badgley, G., Damm, A., Rascher, U., Ryu, Y., Johnson, J., Krieger, V., Wu, S., Qiu, H., Liu, Y., Berry, J.A., Chen, M., 2021. Estimating near-infrared reflectance of vegetation from hyperspectral data. Remote Sens. Environ. 267, 112723.

Zeng, Y., Hao, D., Huete, A., Dechant, B., Berry, J., Chen, J.M., Joiner, J., Frankenberg, C., Bond-Lamberty, B., Ryu, Y., Xiao, J., Asrar, G.R., Chen, M., 2022b. Optical vegetation indices for monitoring terrestrial ecosystems globally. Nat.Rev. Earth Environ. 3, 477–493.

Zhang, X., Liu, L., Chen, X., Gao, Y., Xie, S., Mi, J., 2021. GLC_FCS30: global land-cover product with fine classification system at 30 m using time-series Landsat imagery. Earth Syst.Sci.Data 13, 2753–2776.

Zhang, Y., Guanter, L., Berry, J.A., van der Tol, C., Yang, X., Tang, J., Zhang, F., 2016b. Model-based analysis of the relationship between sun-induced chlorophyll fluorescence and gross primary production for remote sensing applications. Remote Sens. Environ. 187, 145–155.

Zhang, Y., Joiner, J., Alemohammad, S.H., Zhou, S., Gentine, P., 2018a. A global spatially contiguous solar-induced fluorescence (CSIF) dataset using neural networks. Biogeosciences 15, 5779–5800.

Zhang, S., Liu, L., Liu, X., Liu, Z., 2016a. Development of a new BRDF-resistant vegetation index for improving the estimation of leaf area index. Remote Sens. 8, 947.

Zhang, Y., Xiao, X., Zhang, Y., Wolf, S., Zhou, S., Joiner, J., Guanter, L., Verma, M., Sun, Y., Yang, X., 2018b. On the relationship between sub-daily instantaneous and daily total gross primary production: implications for interpreting satellite-based SIF retrievals. Remote Sens. Environ. 205, 276–289.

Zhang, Z., Zhang, Y., Chen, J.M., Ju, W., Migliavacca, M., El-Madany, T.S., 2021b. Sensitivity of estimated total canopy SIF emission to remotely sensed LAI and BRDF products. J.Remote Sens. 2021, 1–18.

Zhang, Z., Zhang, Y., Porcar-Castell, A., Joiner, J., Guanter, L., Yang, X., Migliavacca, M., Ju, W., Sun, Z., Chen, S., Martini, D., Zhang, Q., Li, Z., Cleverly, J., Wang, H., Goulas, Y., 2020. Reduction of structural impacts and distinction of photosynthetic pathways in a global estimation of GPP from space-borne solar-induced chlorophyll fluorescence. Remote Sens. Environ. 240, 111722.

Zheng, Y., Zhang, L., Xiao, J., Yuan, W., Yan, M., Li, T., Zhang, Z., 2018. Sources of uncertainty in gross primary productivity simulated by light use efficiency models: model structure, parameters, input data, and spatial resolution. Agric. For. Meteorol. 263, 242–257.